Study of Monte Carlo Simulation Method for Methane Phase Diagram Prediction using Two Different Potential Models

Thesis by

Ahmad Salim Kadoura

In Partial Fulfillment of the Requirements

For the Degree of

Master of Science

King Abdullah University of Science and Technology

Thuwal, Kingdom of Saudi Arabia

June 2011

The thesis of Ahmad Salim Kadoura is approved by the examination committee.

Committee Chairperson: Shuyu Sun

Committee Member: Klaus –Viktor Peinemann

Committee Member: Zhiping Lai

ABSTRACT

Study of Monte Carlo Simulation Method for Methane Phase Diagram Prediction using Two Different Potential Models

Ahmad Salim Kadoura

Lennard-Jones (L-J) and Buckingham exponential-6 (exp-6) potential models were used to produce isotherms for methane at temperatures below and above critical one. Molecular simulation approach, particularly Monte Carlo simulations, were employed to create these isotherms working with both canonical and Gibbs ensembles. Experiments in canonical ensemble with each model were conducted to estimate pressures at a range of temperatures above methane critical temperature. Results were collected and compared to experimental data existing in literature; both models showed an elegant agreement with the experimental data. In parallel, experiments below critical temperature were run in Gibbs ensemble using L-J model only. Upon comparing results with experimental ones, a good fit was obtained with small deviations. The work was further developed by adding some statistical studies in order to achieve better understanding and interpretation to the estimated quantities by the simulation. Methane phase diagrams were successfully reproduced by an efficient molecular simulation technique with different potential models. This relatively simple demonstration shows how powerful molecular simulation methods could be, hence further applications on more complicated systems are considered. Prediction of phase

behavior of elemental sulfur in sour natural gases has been an interesting and challenging field in oil and gas industry. Determination of elemental sulfur solubility conditions helps avoiding all kinds of problems caused by its dissolution in gas production and transportation processes. For this purpose, further enhancement to the methods used is to be considered in order to successfully simulate elemental sulfur phase behavior in sour natural gases mixtures.

ACKNOWLEDGEMENTS

At first, I would like to thank my supervisor and committee chair, Dr. Shuyu Sun and the committee members, Dr. Zhiping Lai, and Dr. Klaus-Victor Peinemann for their feedback and fruitful criticism to help making this piece decent.

My deep appreciation for the help and support I received from Dr. Shuyu Sun and Dr. Jun Li through the whole process of coding, running experiments and writing.

Finally, my heartfelt gratitude is extended to my parents and my fiancée for their encouragement, care and prayers.

TABLE OF CONTENTS

LIST OF ABBREVIATIONS

APACT	Associating Perturbed Anisotropic Chain Theory
EOR	Enhanced Oil Recovery
EoS	Equations of State
Exp-6	Buckingham Exponentail-6 Model
L-J	Lennard-Jones Model
MC	Monte Carlo Simulation
MD	Molecular Dynamics
NRHB	Non-Random Hydrogen Bonding Theory
PR	Peng-Robinson Equation
SAFT	Statistical Associating Fluid Theory
SRK	Soave-Redlich-Kwong Equation
UA	United Atoms Model
vdW	van der Waals Equation

LIST OF ILLUSTRATIONS

LIST OF TABLES

I- INTRODUCTION

Material properties determination and awareness of phase behaviors of matter represent the core of physical chemistry. For this purpose, plenty of phase diagrams have been constructed for a huge library of substances. Phase diagrams ranging from simple pressure-temperature or P-T phase diagrams for single components to multi-dimensional ones for multiple components. The importance of constructing such diagrams underlies within the clear description of various possible scenarios in which a substance may respond towards different thermodynamic conditions.

Understanding phase behavior and fluid properties of pure components and multi-component systems is essential for various fields and applications. For instance, in oil and gas industry, many approaches have been used and developed to study and model phase behavior among different reservoir fluids including hydrocarbons, water and some of the existing impurities such as sulfur and CO_2. Monitoring phase changes and fluid properties influence the whole production line of oil and gas, starting from reserves estimation and drilling, passing through production and transportation processes till the refinery.

Phase behavior analysis further influences the whole range of the primary, secondary and tertiary Enhanced Oil Recovery (EOR) projects. According to Latil [1], fluid characteristics such as: viscosity, miscibility and saturation are the main contributors in improving production. Therefore, EOR approaches basically utilize the effect of

temperature change [2, 3], injection of polymeric fluids [4, 5], surfactants [6, 7], and different types of gas injection [8-10] to tune these parameters.

Another vivid domain requiring a good knowledge of phase behaviors, which resides a common interest area for both environmental issues and oil industry, is CO_2 sequestration. According to Herzog and Golomb [11], CO_2 sequestration is the process of storing CO_2 gas in a safe and suitable place rather than being emitted to the atmosphere. CO_2 sequestration was firstly proposed to reduce CO_2 concentration in the atmosphere since it is believed to be one of the main contributors to climate change [12] and global warming. CO_2 is mainly sequestrated in saline formations [13] or in oil and gas reserves as an EOR method [14, 15]. In both cases, estimating the thermodynamic conditions for the solubility of CO_2 in storage fluids is critical. In the first case, it guarantees suitable and long term storage while in the second it produces oil more efficiently.

Moreover, the solubility of elemental sulfur during sour gas production has been extensively investigated in order to control its phase transitions. Sulfur is highly soluble in sour gas, but due to pressure and temperature drop accompanying the production process sulfur might precipitate. Even the origin of hydrogen sulfide (H_2S) [16] is group of chemical reactions; still the deposition of sulfur has been proved to be a physical transformation [17] with no chemical reactions involved. Therefore, sulfur deposition has been reported at areas of pressure reduction such as: nozzles connecting pipelines [18] and control valves [19]. In addition to the problems the deposition may cause

during transportation [20], inflow performance depletion [21, 22] may occur as the sulfur accumulates at the reservoir rock itself.

In this study, Monte Carlo (MC) simulation was employed to construct phase diagrams for methane gas using two self generated codes in Fortran95 working with Canonical and Gibbs ensemble. Phase diagrams obtained from L-J model and exp-6 model were compared to determine the suitable model to be used. Based on this work, a milestone is established to extend the investigations and conduct further studies on solubility of different elemental sulfur allotropes in sour gas reservoirs.

In the following section, a clear discussion and review about each of the recent approaches in phase behavior predictions will be provided in terms of theory and application. The author will be focusing more on molecular simulation technique and MC method in specific as being the method used to obtain results. An extensive explanatory section for the experimental work and progress will follow the theoretical part, to end by summing up all the results in a brief conclusion after screening and discussion.

II- LITERATURE REVIEW

In literature, several techniques and approaches have been introduced and developed to study phase behaviors and substances properties in a wide range of applications and fields. In this section, a brief explanation of each approach and some of its corresponding work conducted in literature will be provided. Mainly three types of models are extensively used, namely empirical correlations based on experimental data, equations of state (EoS) models and molecular simulation ones or different combinations of all.

Before starting the discussion about each of these techniques, it is necessary to mention some of the recorded experimental data collected by different groups over years. These experimental data are important in the sense of developing models and comparing results.

1. Experimental Measurements:

As a specific example in our domain of interest, solubility of sulfur, the following table gives a brief historical review of the experiments conducted by several groups, as early as 1960, to obtain sulfur solubility in some pure solvents [23-28] (Table 1) and synthetic sour gas mixtures [26, 27, 29-31] (Table 2) at various ranges of temperatures and pressures.

Group	Solvent	Temperature (K)	Pressure (MPa)	Year	Reference
Kennedy and Wieland	CH_4 ,CO_2, H_2S	339, 367 & 394	6.9 – 41	1960	[23]
Roof	H_2S	317 – 394	7 – 31	1971	[24]
Swift et al.	H_2S	390 – 450	35 – 140	1976	[25]
Burnner and Woll	H_2S	373 – 433	10 – 60	1980	[26]
Gu et al.	CH_4 ,CO_2, H_2S	363 – 383	12 – 50	1993	[27]
Migdisov et al.	H_2S	323 – 563	0.5 – 20	1998	[28]

Table 1: Experimental Studies for the Solubility of Solid Sulfur in Pure Solvents.

Group	H_2S (%)	Temperature (K)	Pressure (MPa)	Year	Reference
Burnner and Woll	1 – 20	373 – 433	10 – 60	1980	[26]
Burnner et al.	9 – 84	393 – 485	7 – 155	1988	[29]
Davis et al.	Up to 90	333, 363, 393 & 423	5 – 55	1992	[30]
Gu et al.	44 – 95	363	20 – 45	1993	[27]
Sun and Chen	5 – 27	303 – 363	10 – 35	2003	[31]

Table 2: Experimental Studies for the Solubility of Solid Sulfur in Synthetic Sour Gas Mixtures.

Solubility of sulfur in H_2S or in other reservoir fluids was not the only target of the experimental work. Scientists were also interested to model the solubility of H_2S [32-36] itself in water, to develop better awareness of other phase changes during production processes. Again, and as stated in the introduction, phase behavior and equilibria studies are involved in many fields, and in each of these fields the experimental data [37] collection is an indispensible step.

2. Empirical Models:

Density based empirical models and some other semi-empirical ones are used frequently to model the solubility of different solutes in supercritical solvents. They are preferable for their ease and simplicity in application. However, it is very common to be coupled with EoS [38-40] to target higher accuracy with some more difficulty in manipulation. The first empirical model was proposed by Charstil [41] to correlate solubility of liquids and solids in supercritical gases. Later on, many other models have been developed by adding some modifications.

Chrastil model [41] (1982):

$$lnS = C_1 + \frac{C_2}{T} + K ln\rho \quad (1)$$

Modified Chrastil model by del Valle and Aguilera [42] (1988):

$$lnS = C_1 + \frac{C_2}{T} + \frac{C_3}{T^2} + K ln\rho \quad (2)$$

Where *C*'s and *K* are correlation parameters, *S* is solubility, *ρ* is density.

As year passed, more and more models were developed and used in various fields, for example: Kumar and Johnston [43] model, Mendez-santiago-Teja [44] model and Bartle [45] model. The literature is full of experimental data collected for the solubility of a long list of solutes in supercritical CO_2 [46-49] that have been correlated with the help of

these and other similar empirical and semi-empirical models as well as the solubility of sulfur[22, 50] in sour gas mixtures.

3. Equations of State:

An equation of state (EoS) presents a relation among state functions or variables which are dependent on the current state of the system regardless of the path it passed to reach it. These state variables are generally pressure (P), volume (V) and temperature (T). Therefore, a general EoS is a function of P, V and T. Ideal gas law is the simplest ever known EoS, where both interaction of gas molecules with each other and the surrounding walls are neglected.

General Equations of State:

$$F(P,V,T) = 0 \tag{3}$$

Ideal Gas Law:

$$PV = nRT \tag{4}$$

Where n is number of moles and R is a constant. R should be consistent with the system of units used.

3.1. Cubic Equations of State:

The first breakthrough in EoS development came with the van der Waals (vdW) [51] equation of state. Since that time 1873, huge number of equations of state has been

formulated, however cubic EoS preserved a special rank by being widely used in numerous fields. Particularly, in petroleum and chemical [17, 27, 52] engineering both Soave-Redlich-Kwong (SRK) [53] and Peng-Robinson (PR) [54] are the most used.

Van der Waals (vdW) EoS [51]:

$$P = \frac{RT}{V-b} - \frac{a}{V^2} \tag{5}$$

Soave-Redlich-Kwong (SRK) EoS [53]:

$$P = \frac{RT}{V-b} - \frac{a(T)}{V(V+b)} \tag{6}$$

Peng-Robinson (PR) EoS [54]:

$$P = \frac{RT}{V-b} - \frac{a(T)}{V(V+b) + V(V-b)} \tag{7}$$

Where a and b are model parameters and substance related.

Cubic EoS and some modified cubic EoS showed tremendous capabilities and were so beneficial vapor liquid phase equilibria, predicting vapor pressures, saturation and critical properties [55-59]. As for the solubility of sulfur and elemental sulfur phase behavior predictions in sour natural gas fields, PR equation was extensively used starting from 1988 [60]. Later on, other groups have investigated sulfur with different model parameters based on PR equation [52, 61]. Elemental sulfur deposition in pipelines was modeled too [17] using PR equation coupled with some classical constitutive, mass balance and energy balance equations to prove the physical nature of such process. In

2003, Chen and Sun [31] conducted experiments on solubility of sulfur at a wide range of pressures and temperatures. They correlated their data by a modified PR equation; however their success was limited.

Other problems were still faced while utilizing cubic EoS, especially in applications dealing with complex systems, including highly immiscible components such as water-alkanes, hydrogen bond or electrolytes containing compounds. To overcome these challenges, higher order EoS concept was introduced.

3.2. Higher Order Equations of State:

Higher order EoS found their way gradually to the industrial applications [62-69] in the last three decades, and created a powerful tool when combined to the conventional EoS. The concept of these equations was basically built up on statistical mechanics principles. Many families of higher order EoS were derived including Associated Perturbed Anisotropic Chain Theory (APACT) [70, 71], Non-Random Hydrogen Bonding (NRHB) [72] theory for pure and multi-component mixtures [73] based on lattice theory [74], and the Statistical Associating Fluid Theory (SAFT) [75, 76] with all its derivatives such as: soft-SAFT [77], PC-Polar SAFT [78], electrolyte SAFT [79, 80].

4. Molecular Simulation:

Molecular simulation [81] is based on the principle of statistical thermodynamics and quantum chemistry methods, which provide a link between microscopic properties of a matter and its bulk ones. In other words, molecular simulation intends to determine

thermophysical properties of a certain system by closely studying the molecular behavior and interactions of an extremely small size system in few nanometers scale. Generally speaking, two methods have been developed so far to run molecular simulations, Monte Carlo (MC) simulation and Molecular Dynamics (MD).

4.1. Statistical Ensembles:

The first step towards introducing the molecular simulation technique and statistical mechanics is to define the statistical ensemble concept. Statistical ensembles refer to all possible states a system can attain under certain imposed parameters. Each ensemble represents the experimental domain or space while a large number of configurations is created within, in order to determine some of the system properties. In general, six ensembles [82] could be categorized according to their imposed set of constraints and probability densities. The choice of the suitable ensemble to work with mainly depends on the desired application. In this study we are only interested in employing both canonical and Gibbs ensembles.

4.1.1. Canonical ensemble:

This ensemble is the simplest in terms of structure and usually used to determine phase properties. Number of molecules, volume and temperature are all imposed and kept constant throughout the whole simulation process. On the other hand, the energy of the system is allowed to fluctuate and change from one configuration to another. However, the change of energy is controlled by the probability density; this idea will be

further discussed in the experimental section under the "Trial move acceptance condition" concept.

4.1.2. Gibbs Ensemble:

In Gibbs ensemble [83] different separated simulation boxes are created to deal with systems of two phases. Practically, Gibbs ensemble can be divided into two types. In the first, the global volume of boxes and global number of molecules in all boxes are fixed, while molecule swapping between boxes and individual box's volume change is allowed; the temperature is imposed too. In the second one, only the global number of molecules is imposed while global volume is unconstrained. In addition to temperature, the pressure is kept fixed. The nature of the application is the key behind choosing the suitable ensemble. In this study, since we are dealing with pure methane, the Gibbs ensemble at imposed global volume was chosen.

4.2. Molecular System's Energy:

The energy term E included in the probability density formula expresses the total energy of the system as kinetic and potential. The kinetic energy is analytically solvable, so only the potential term needs to be explicitly provided for both MC and MD methods. The potential energy is gained by a system due to two types of interactions, intermolecular interactions among different molecules and intramolecular interactions between different atoms or groups within the same molecule itself. Based on this fact, the

potential energy could be expressed as a summation of two terms each obtained from a different source.

4.2.1. Intermolecular or External Potential Energy:

Intermolecular or external potential energy (U_{ext}) is further segregated into polarization energy (U_{pol}), electrostatic or columbic interaction energy (U_{col}) and dispersion-repulsion interaction energy ($U_{d\text{-}r}$). Practically dispersion-repulsion interactions are the dominant, while electrostatic interactions count for polar molecules only.

Intermolecular Energy:

$$U_{ext} = U_{d-r} + U_{col} + U_{pol} \tag{8}$$

Columbic Energy:

$$U_{col} = \sum_{\substack{i,j \\ i<j}} \frac{1}{4\pi\varepsilon_o} \frac{q_i q_j}{r_{ij}} \tag{9}$$

Dispersion-Repulsion Energy in Different Models:

Lennard-Jones (L-J) Model [84]:

$$U_{LJ}(r) = \sum_{\substack{i,j \\ i<j}} 4\varepsilon_{ij} \left(\left(\frac{\sigma_{ij}}{r_{ij}} \right)^{12} - \left(\frac{\sigma_{ij}}{r_{ij}} \right)^{6} \right) \tag{10}$$

Buckingham Exponantial-6 (exp-6) Model [85] :

$$U_{exp-6}(r) = \begin{cases} \sum_{\substack{i,j \\ i<j}} \frac{\varepsilon_{ij}}{1-\frac{6}{\alpha_{ij}}} \left[\frac{6}{\alpha_{ij}} \exp\left(\alpha_{ij}\left[1-\frac{r_{ij}}{r_m}\right]\right) - C_{ij}\left(\frac{r_m}{r_{ij}}\right)^6 \right] & for\ r > r_{max} \\ \infty & for\ r < r_{max} \end{cases} \quad (11)$$

With these notations the energies express the sum of all the possible interactions between any two molecules *i* and *j*. Where *q* is the charge, *r* is the separation distance, ε_o = 8.85419x10^{-12} C^2/Nm^2, *α, σ, ε and C* are model parameters related to the nature of molecule used and their averages are taken for different molecules consideration. r_m and r_{max} are distance of minimum potential occurrence and cutoff distance respectively. U_{pol} usually evaluated based on experimental data.

4.2.2. Intramolecular or Internal Potential Energy:

Internal Potential Energy (U_{int}) is a result of the variation in bond length or the bending angle (U_{bend}) which is formed by two consecutive bonds. In addition to the bending energy, torsion energy (U_{tor}) is considered due to possible rotations within molecules along three successive bonds leading to a variation in the so called "dihedral angel". Moreover, non-polar interactions between atoms or groups within the same molecule can be accounted by either L-J or exp-6 models introduced earlier. In real applications, stretching, bending and torsion contributions are neglected for rigid molecules.

Intramolecular Energy:

$$U_{int} = U_{bend} + U_{tor} + U_{d-r} \quad (12)$$

Bending Energy:

$$U_{bend} = \frac{K_\theta}{2}(\theta - \theta_o)^2 \quad (13)$$

Or

$$U_{bend} = \frac{K'_\theta}{2}(\cos(\theta) - \cos(\theta_o))^2 \quad (14)$$

Torsion Energy:

$$U_{tor} = \sum_{k=0}^{8} a_k cos^k(\emptyset) \quad (15)$$

Where θ and θ_0 are measured and equilibrium bending angles respectively, ϕ is the dihedral angle, K_θ and K'_θ are constants, a_k's are material dependent parameters.

4.3. Molecular Simulation Technique:

As have been stated earlier, two main methods to simulate these statistical ensembles are used, namely Monte Carlo (MC) simulations and Molecular Dynamics (MD). And again, the choice between the two methods mainly depends on the targeted property or parameter. Typically, both are used to determine equilibrium properties of fluid by computing the arithmetic average of the property with respect to the number of created configurations. Whenever dealing with fluid phase equilibria, MC is recommended. However MD is preferable and proved to be more efficient in determining time dependent properties such as transport coefficients.

4.3.1. Monte Carlo Simulation:

According to MC scheme, a large number of configurations is generated by creating some trial moves within or among simulation boxes. Even the type and the size of each move is randomly chosen, still not all trial moves are accepted. The judging criterion or the acceptance condition for any newly generated configuration is constrained by the probability distribution of each ensemble. For instance the acceptance condition for canonical ensemble is: $e^{-\beta \Delta U} > 1$ where β is the Boltzmann's factor and ΔU is change in systems potential energy due to MC move.

4.3.1.1. Types of Trial Moves:

Trial move [86] represents the step taken when moving from one configuration to another. The list of the possible trial moves that may reconfigure the particles in a simulation box or boxes is long. Main trial moves in general can be summarized into two categories (Figure 1), moves within the same simulation box and could be translation, rotation or partial regrowth and moves between different simulation boxes, representing different phases as in Gibbs ensemble case, and could be volume changes or molecules swapping.

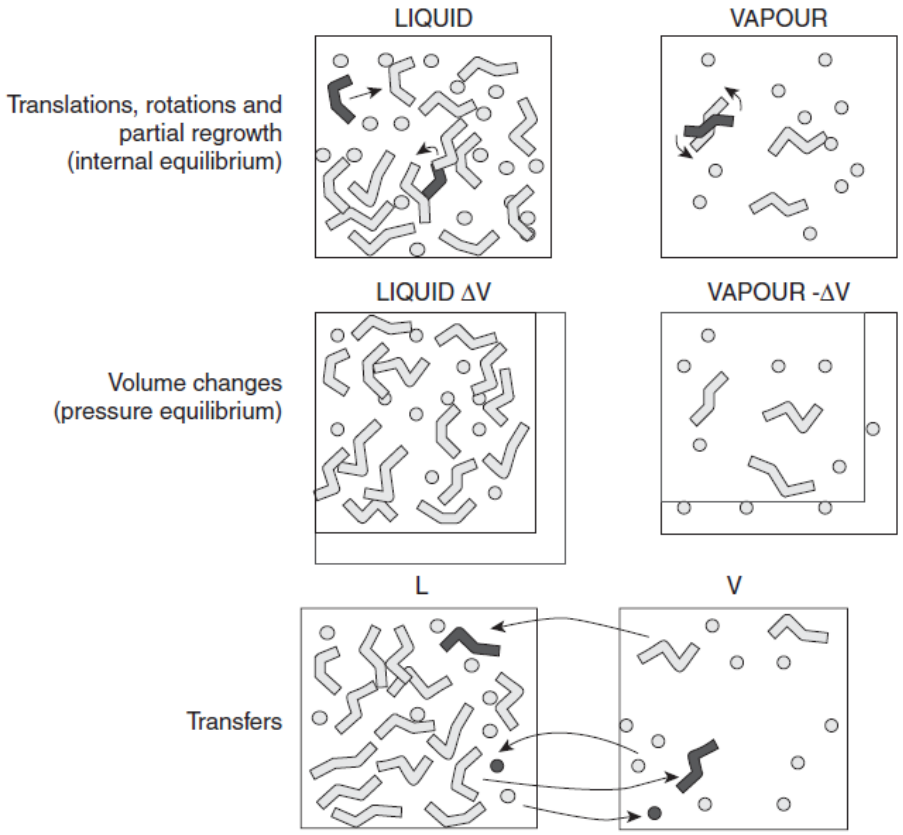

Figure 1: Types of Trial Moves [86] for Both Canonical (Only First One) and Gibbs Ensembles.

4.3.1.2. Monte Carlo Applications:

A numerous number of studies and research have been conducted utilizing MC method. In most cases, Gibbs ensemble was simulated to examine phase equilibrium properties of pure components and mixtures. For this purpose a wide range of potential models have been developed and coupled to suit certain fields of application or to improve accuracy. Gibbs ensemble was first implemented in MC simulation in 1987 by Panagiotopoulos [83]. Later on, Panagiotopoulos et al. have developed other ensembles [87] and potential models [88-90] to extend their phase equilibria studies conducted by MC method and enhance its accuracy [91-96].

4.3.2. Molecular Dynamics Method:

MD is time dependent scheme. It investigates the physical movement of the particles by numerically solving Newton's equations of motion for every particle existing in the system. MD was employed in different sections of science and engineering such as: chemistry [97], physical chemistry [98-100] and molecular biology [101]. MD is out of the scope of this work since it will not be implemented, so this was just a small insight about it.

III- EXPERIMENTAL WORK AND PROCEDURE

1. Methane Molecule Representation:

Methane molecule is a non-polar symmetric molecule made of a central carbon atom covalently bonded to four hydrogen atoms forming a tetrahedral structure. Being a non-polar molecule, no columbic effects are to be considered and only the dispersion intermolecular interactions exist. For further simplicity, the "United Atoms" or UA model [102] is used to describe each methane molecule. According to UA convention, the force center represents a group of atoms (The carbon and the four hydrogen atoms bonded to it) and is located at the center of the central atom (Carbon atom). Therefore, each methane molecule is represented by a point in the simulation box and the only type of interaction possible is the dispersion intermolecular interaction. The experiments are done in canonical and Gibbs ensembles using both L-J and exp-6 model.

2. Simulation Box:

The first step in building either canonical or Gibbs ensemble is the creation of the simulation box. The simulation box is the imaginary space or lab where experiments are conducted and results are collected. For canonical ensemble, one cubic box with certain side length "L" is created. This box will be called from now on by the "main box". Following main box creation, "N" number of points are assigned with three X, Y and Z coordinates within the main box borders. As discussed earlier, each point will be

representing a methane molecule. In Gibbs ensemble, the experiment starts with two separate main boxes with same volume and including same number of particles. In the latter, two boxes are needed to simulate the phase separation. In all the experiments conducted, the initial configuration of the particles was uniform.

3. Periodic Boundary Conditions:

In an extremely small system, as the one considered in this work, the boundary effects are significant and cannot be simply neglected. For this purpose, periodic boundary conditions (Figure 2) were imposed in order to mimic the presence of an infinite bulk surrounding the main box created. This is achieved by creating infinite identical images of the main box surrounding it from all directions. Therefore, a particle "i" in the main box not only interacts with the particles sharing it the main box space, but also the images surrounding it including its own image. However, in practice only the nearest 27 boxes surrounding the main box were generated in the code by truncating the effect of far particles.

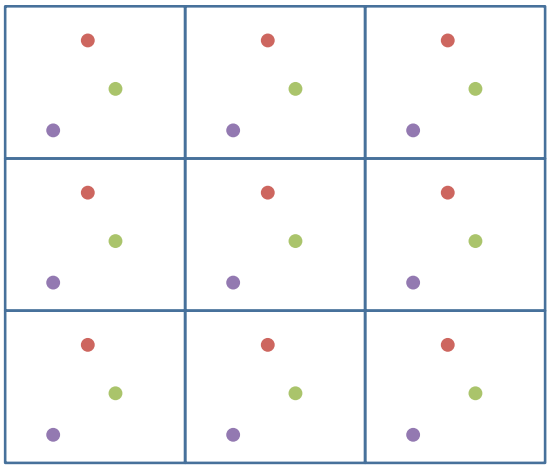

Figure 2: Main box images created by periodic boundary conditions convention.

4. Truncation of Interaction:

The interaction between any two particles is inversely proportional to the separation distance between them. Based on this fact, the interaction among the particle under interest and the other particles at a further distance than a cutoff radius "r_c", is considered negligible compared to the contribution of the other neighboring particles. The simplest way of truncation works by totally neglecting the interactions of the particles situated at a distance further than r_c from the picked particle. In the developed code, the value of r_c was 0.45*L; as a result it is impossible for the particles settling outside the nearest 27 boxes to the main box to contribute to any of the particles within the main box itself. However, disposed interactions due to truncation must be corrected by adding a tail function to both energy and pressure separately.

5. Energy, Pressure and Tail Corrections:

In canonical as well as Gibbs ensembles pressure and total energy of the main box are affected by the truncation assumption. The pressure is evaluated as being the quantity targeted and the total energy of the main box is required in order to judge whether the trial move generated is to be accepted or not.

5.1. Main Box Energy:

The average potential energy [81] for any given particle i in three dimensions is:

$$u_i = \left(\frac{1}{2}\right) \int_0^\infty 4\pi r^2 \rho(r) u(r)\, dr \qquad (16)$$

Where *ρ(r)* is the average number density at a distance *r* from the particle and *u(r)* is the pair potential. Number density is assumed constant and equal to the total density of main box. The half factor is used to eliminate the double counting for interactions.

According to the definition above, the truncated contributions to be corrected by the tail function can be expressed as:

$$u_{tail} = \left(\frac{1}{2}\right) 4\pi\rho \int_{r_c}^{\infty} r^2 u(r)\, dr \tag{17}$$

5.1.1. L-J Model Potential Energy Tail Function:

The average potential energy for one particle modeled by L-J:

$$u(r) = 4\varepsilon \left[\left(\frac{\sigma}{r}\right)^{12} - \left(\frac{\sigma}{r}\right)^{6} \right] \tag{18}$$

Substituting this in (16) and integrating over the specified interval, the tail function for energy modeled by L-J will be:

$$u_{tail} = (8/3)\pi\rho\varepsilon\sigma^3 \left[\left(\frac{\sigma}{r_c}\right)^{12} - \left(\frac{\sigma}{r_c}\right)^{6} \right] \tag{19}$$

5.1.2. Exp-6 Model Potential Energy Tail Function:

The average potential energy for one particle according to exp-6 model:

$$u(r) = \left(\frac{\varepsilon}{1 - \frac{6}{\alpha}}\right) \left[\frac{6}{\alpha} \exp\left(\alpha \left[1 - \frac{r}{r_m}\right]\right) - C \left(\frac{r_m}{r}\right)^{6} \right] \tag{20}$$

Plugging into (16) and integrating twice by parts the resultant will be:

$$u_{tail} = 2\pi\rho r_m^3 \left(\frac{\varepsilon}{1-\frac{6}{\alpha}}\right)\left[\frac{6}{\alpha^4}e^{\alpha\left(1-\frac{r_c}{r_m}\right)}\left(\alpha^2\left(\frac{r_c}{r_m}\right)^2 + 2\alpha\left(\frac{r_c}{r_m}\right)+1\right) - \frac{C}{3}\left(\frac{r_m}{r_c}\right)^3\right] \quad (21)$$

Noting that in both cases only the r_c term survived; as r tends to infinity, in the case of the L-J model the reciprocal of r tends to zero and vanishes. In the case of exp-6 model, the same result is reached and can be proved in the presence of the exponential term, by some manipulation of "L' Hopital rule".

5.2. Main Box Pressure:

The pressure of the main box is evaluated using the viral (Vir) function [81]:

$$P = \left(\frac{\rho}{\beta}\right) + \left(\frac{Vir}{V}\right) \quad (22)$$

Where β is the Boltzmann's factor and the viral function is expressed as:

$$Vir = \left(\frac{1}{3}\right)\sum_i \sum_{j>i} f(r_{ij}).r_{ij} \quad (23)$$

Or more explicitly:

$$Vir = \left(\frac{1}{3}\right)\sum_i \sum_{j>i} -\left(\frac{\partial u_{ij}}{\partial r_{ij}}\right) r_{ij} \quad (24)$$

Consequently, the pressure correction can be evaluated by the following formula:

$$P_{tail} = \left(\frac{1}{2}\right) 4\pi\rho^2 \int_{r_c}^{\infty} r^2 (-\frac{du}{dr} r) dr \quad (25)$$

5.2.1. L-J Model Pressure Tail Function:

$$P_{tail} = (16/3)\pi\rho^2\varepsilon\sigma^3 \left[\left(\frac{2}{3}\right)\left(\frac{\sigma}{r_c}\right)^9 - \left(\frac{\sigma}{r_c}\right)^3 \right] \quad (26)$$

5.2.2. Exp-6 Model Pressure Tail Function:

$$P_{tail} = \left(\frac{12}{3}\right)\pi\rho^3 r_m^3 \left(\frac{\varepsilon}{1-\frac{6}{\alpha}}\right) \left[\frac{e^{\alpha\left(1-\frac{r_c}{r_m}\right)}}{\alpha} A - \frac{C}{3}\left(\frac{r_m}{r_c}\right)^3 \right] \quad (27)$$

Where:

$$A = \left(\frac{r_c}{r_m}\right)^3 + \left(\frac{3}{\alpha}\right)\left(\frac{r_c}{r_m}\right)^2 + \left(\frac{6}{\alpha^2}\right)\left(\frac{r_c}{r_m}\right) + \left(\frac{6}{\alpha^3}\right) \quad (28)$$

6. Normalization:

Numerically speaking, it is unsafe to deal with big numbers in value while simulating. For that reason all the variables are normalized with respect to the model parameters corresponding to the chemical nature of the particles used (Table 3).

Parameter	Normalizing Unit
Length	σ or r_m
Energy	ε
Temperature	ε/K_B
Pressure	ε/σ^3

Table 3: Normalizing units and their corresponding parameters.

Noting that, the only difference between the two potential models in terms of normalization is in the unit of length; where L-J model is normalized by σ and exp-6 is normalized by r_m (Table 4).

Model Parameter	L-J Model	Exp-6 Model
σ (A)	3.723	3.741
r_m (A)	-	4.188
ε/K_B (J)	147.0	160.3
α	-	15
C	-	1

Table 4: Parameters used for methane corresponding to each model [103].

7. Trial Moves and Acceptance Conditions:

It is clear by assuming each methane molecule as a point that all the intramolecular interactions lost their significance. In other words, the trial moves related to molecular geometry modification, such as bending and torsion, are not possible. On the other hand, the only possible moves are the ones related to the position of the molecule.

7.1. Translational Move:

A particle is chosen randomly from the main box or one of the main boxes (In Gibbs ensemble case). The chosen particle is moved by a random step size which could be regulated. However, if it happened and the particle left the main box imaginary borders, the particle is returned back to the main box from the opposite side with the same increment it left. After the movement generation and position regulation, the

change in the total potential energy of the main box due to this translation is calculated. The move is accepted if, and only if, the following acceptance condition is satisfied.

Translational acceptance condition:

$$e^{-\beta \Delta U} \geq RF \tag{29}$$

Where *RF* is a random number between 0 and 1, this implies that a move is accepted if the potential energy of the box decreased due to the particle translation, or if it slightly increased.

7.2. Volume Change:

This trial move is not used in the canonical ensemble; the volume of one of the boxes is changed by a randomly chosen ratio, and the other box is changed in a way that the total volume of the two main boxes is conserved.

Volume change acceptance condition:

$$R_1^{n_1+1} R_2^{n_2+1} e^{-\beta \Delta U} \geq RF \tag{30}$$

Where *R* and *n* represents the ratio of volume change and number of particles for each of the main boxes respectively, also to be noted here that the change in potential energy is meant to be the change in total energy of the whole system (for both boxes).

7.3. Particle Swapping:

Again this move is exclusive to the Gibbs ensemble in this particular work. In this trial, a main box is randomly chosen at first and then a randomly chosen particle from the box is moved to the other. The particle is assigned to a totally new random position in the other box. The change in the total energy of the two boxes determines the acceptance.

Swapping acceptance Condition:

$$\frac{n_{out}V_{in}e^{-\beta\Delta U}}{(n_{in}+1)V_{out}} \geq RF \tag{31}$$

Where *n* and *V* represents the number of particles and volume in each of the boxes before swapping. "in" and "out" indices were used to differentiate from which box the particle was moved out and to which was placed in.

8. Evaluating System's Total Potential Energy Change:

Due to any of the trial moves listed above, a change in the total energy of the system occurs. According to the magnitude of this change, it is decided whether the move is accepted or not. If accepted the new pressure is recorded for the corresponding iteration and if rejected the previous pressure is recorded and the system's previous configuration is retrieved. When a randomly chosen particle is transferred or swapped, there is no need to revaluate the total energy of the whole system again, since only the distances related to this particle or to its images will change. Consequently, only the change in the energy related to that group of sub energies reflects the total change.

As an illustration, consider a system made of only three particles. Assuming particle "1" was moved to a new position within the main box. As a result, the change in energy due to particle "1" translation can be expressed as:

$$\Delta U_{tot} = \Delta U_1 = \left(\frac{1}{2}\right)(\Delta U_{12} + \Delta U_{13} + \Delta U_{31} + \Delta U_{21}) + \left(\frac{1}{2}\right)[\,(\Delta U_{11'} + \Delta U_{12'} + \Delta U_{13'} + \Delta U_{21'} + \Delta U_{31'}) + \cdots + (\Delta U_{11^{27}} + \Delta U_{12^{27}} + \Delta U_{13^{27}} + \Delta U_{21^{27}} + \Delta U_{31^{27}})\,] \quad (32)$$

The half factor is used to cancel duplication in counting, since we are only interested in evaluating main box's energy change. Geometrically, it is clear that the potential between pairs are equal ($\Delta U_{12} = \Delta U_{21}$). The half factor could be dropped for interactions among particles inside the main box by counting only for one corresponding pair potential rather than two of them. In addition, and by more careful geometrical examining (Figure 3) it is true that the images contributions can be expressed by one term rather than two leading to further simplification in total energy difference evaluation.

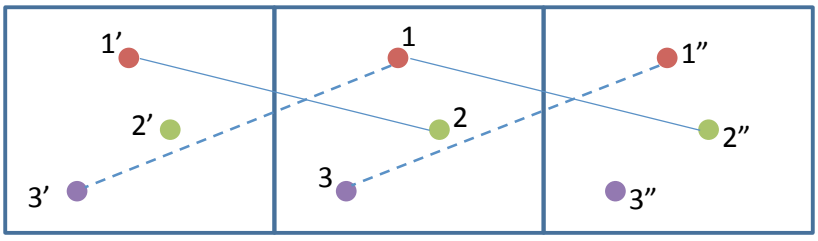

Figure 3: Careful geometrical analysis showing that $\Delta U_{12''} = \Delta U_{21'}$ (Solid line) and $\Delta U_{13'} = \Delta U_{31''}$ (Dashed line).

Thus, most simplified and efficient formula to calculate energy change corresponding to a particle position change is formulated as:

$$\Delta U_{tot} = \Delta U_i = (\Delta U_{i1} + \Delta U_{i2} + .o. + \Delta U_{iN}) + (\Delta U_{i1'} + \Delta U_{i2'} + .o. + \Delta U_{iN'}) \ldots$$
$$+ (\Delta U_{i1^{27}} + \Delta U_{i2^{27}} + .o. + \Delta U_{iN^{27}}) \quad (33)$$

Where, ".o." notation means counting contribution with all particles and their images except its own. Note that, the contribution terms of the corresponding images of the chosen particle "i" were removed, since the distance between a particle and any of its images is greater than r_c, hence it is truncated.

IV- RESULTS AND DISCUSSION

1. Experimental Set I: Optimum Number of Particles (N) Determination

The perfect experiment means respecting both high accuracy and reasonable running time. For this purpose, the choice of the initial number of particles (N) situated in the simulation box is critical. In this experimental set, ten experiments were conducted each at different N values ranging from 100 to 1000 and the normalized pressures ($P^* = P\sigma^3/\varepsilon$) were collected (Appendix, Figures I.1) for 10 million iterations at T = 220 K and normalized number density ($Rho^* = N_A\rho\sigma^3/M_{meth}$) of 0.5407. The CPU time required by each of the systems to complete 10,000 iterations was measured (Figure 4) and found to be linearly related to the particles number. It is important to mention here, that the efficient time dependency achieved is due to the powerful technique used to evaluate system's energy discussed earlier.

Moreover, percentage error of P* obtained by simulation was evaluated with respect to real data available [104]. It was found that, the error has decreased sharply at the first section with the increase of number of particles. According to this result, the percentage error starts to be acceptable (Figure 5) at N values equal and above 300. Noting that, the fluctuation in errors obtained after N = 300 is due to the uncertainty concept during P* estimation which will be further explained in third experimental set. As an optimum choice, and taking into consideration both accuracy and CPU time, it was decided to set N to 500 as a default value for all conducted experiments.

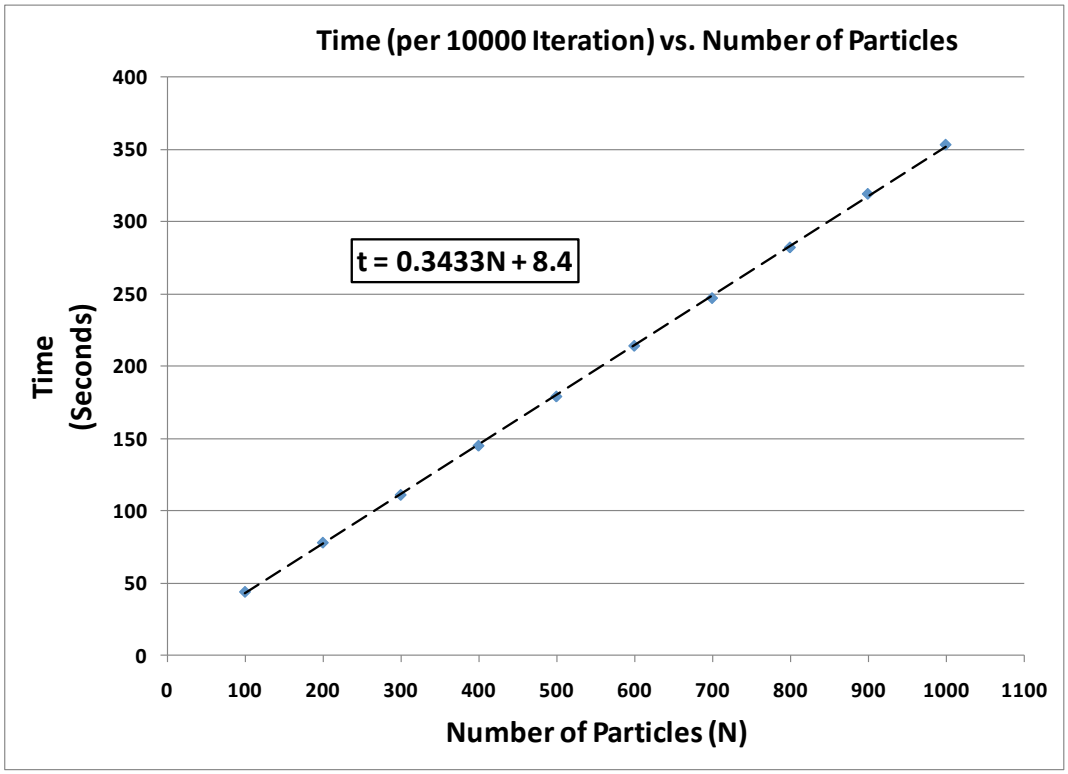

Figure 4: CPU time required to complete 10,000 iterations for different N values.

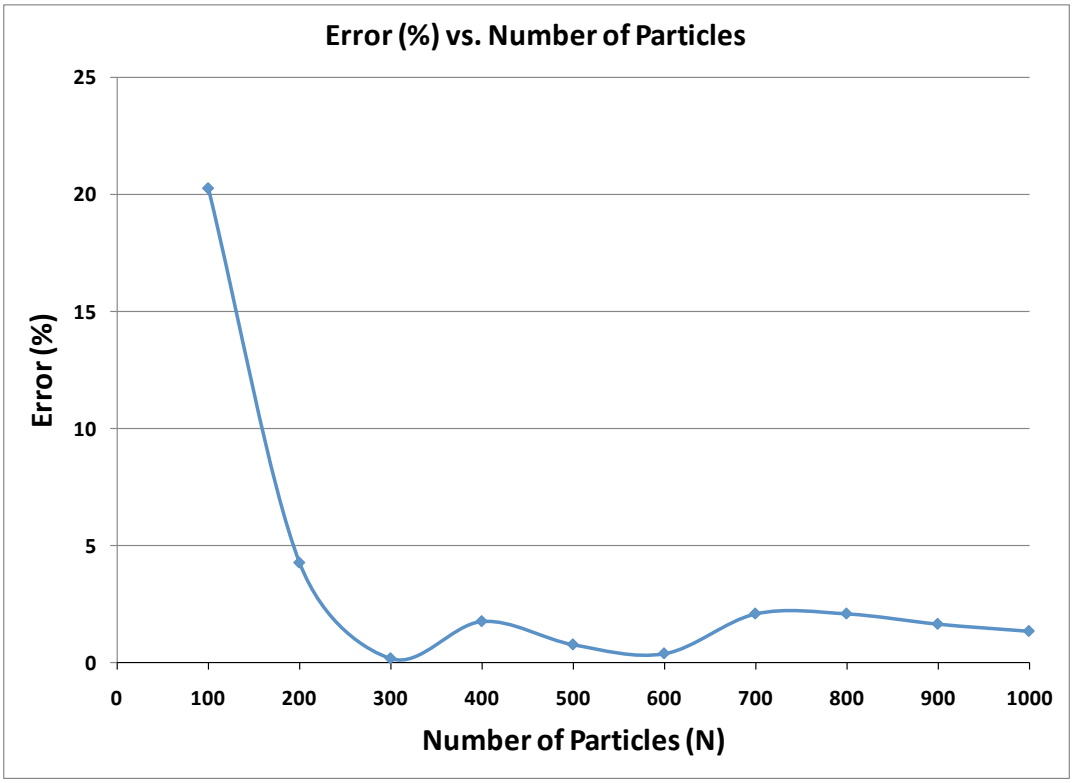

Figure 5: Percentage Error in evaluating P* at different values of N.

2. Experimental Set II: Methane Isotherms above Critical Temperature Using L-J Model in Canonical Ensemble

Pressures of methane were obtained at different densities and a temperature range above critical temperature (T_c = 190.56) from 200 K to 400 K. At each temperature four pressures corresponding to four different densities were evaluated utilizing the canonical ensemble code with the L-J potential model. Plots generated by the code (Appendix, Figures II.1-5) show the normalized pressure values (P*) collected at each iteration. After convergence, the average P* is evaluated with respect to the number of iterations. The P* value obtained represents the simulation estimation for the methane pressure under the temperature and density specified. Collected P* and their corresponding real values of pressures were tabulated (Appendix, Table II.1). Moreover, the percentage error between our simulation results and experimental data collected by Setzmann and Wagner [104] are included.

In order to visualize the results in a clear fashion (Figure 6), the P* estimated by the simulation were plotted versus the expected P* by the experimental data of Setzmann and Wagner [104]. There is no doubt that our results showed a strong agreement with the real values. By examining the plots carefully, a general trend of the values was deduced; at lower temperatures or in other words at temperatures closer to the critical temperature the deviations increased. In addition, it was observed that at same isotherm as density increases the error percentage increases. As a result, 300 K and 400 K isotherms showed an elegant fit to the experimental data curves.

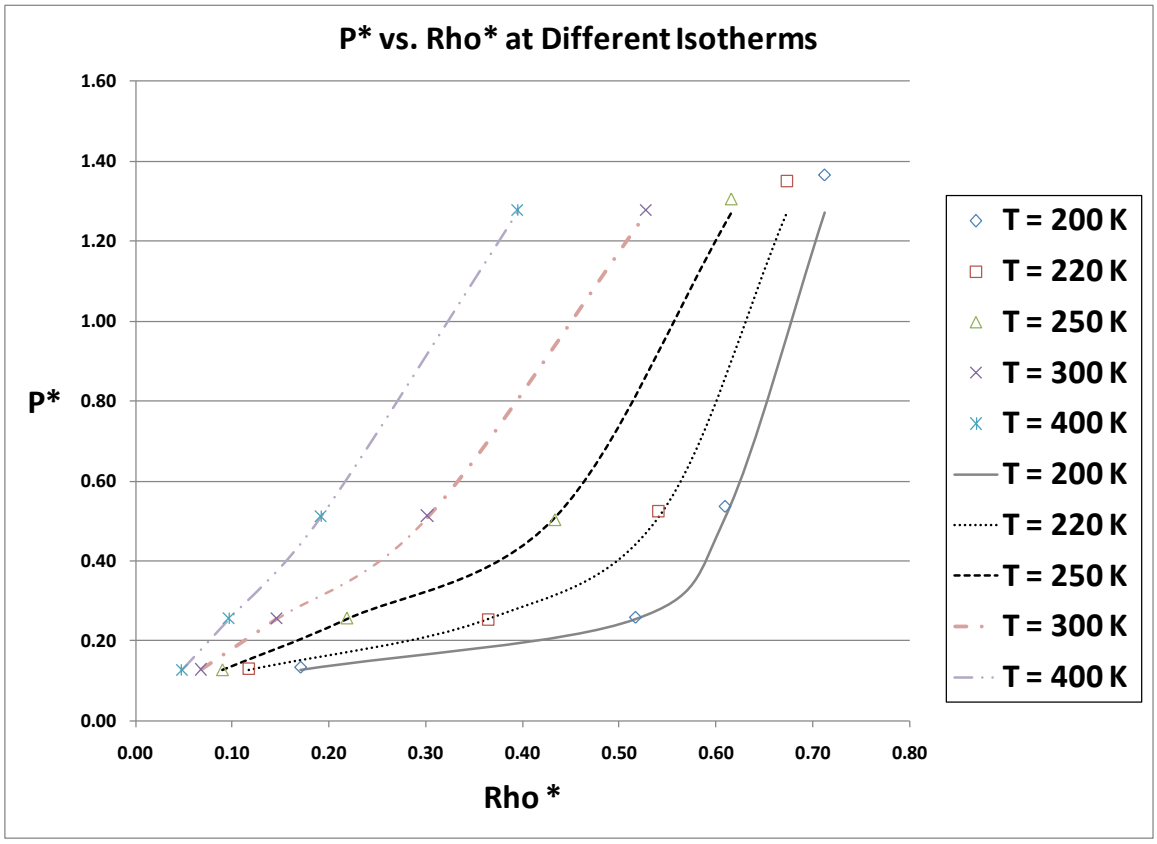

Figure 6: Normalized pressures obtained by L-J model (Symbols) compared to experimental isotherms plots (Lines).

3. Experimental Set III: Variance Studies at Large Number of Iterations

In this part, statistical analysis [105] was carried out in order to have more insight about the validity of the average P* estimated. The deviation from the real data is not merely the responsibility of the potential model used; hence part of it, is technical. The technical part here corresponds to the uncertainty in average P* estimations, since even after convergence the system keeps fluctuating around the true value in both negative and positive directions. In total six experiments (Appendix, Figures III.1-6) were run at T = 220 K and normalized density of 0.5407 for 16, 17, 18, 19, 20 and 23 block sets (MBL). Fifty times of 2^{MBL} iterations were run after 20 million ones to insure convergence (Total

number of iterations = $20*10^6 + 50*2^{MBL}$). The uncertainties in determining the average value P* estimated by the simulation (Figure 7) decreased exponentially as the MBL factor increased. Uncertainty evolution plots (Figures 8) along number of block sets used, started to converge with MBL factors above 19. With MBL = 20 the convergence (Figure 9) was not smooth as in the case of 23, even though it was used to construct uncertainty plots for P* evaluated at T = 220 K but at four different densities.

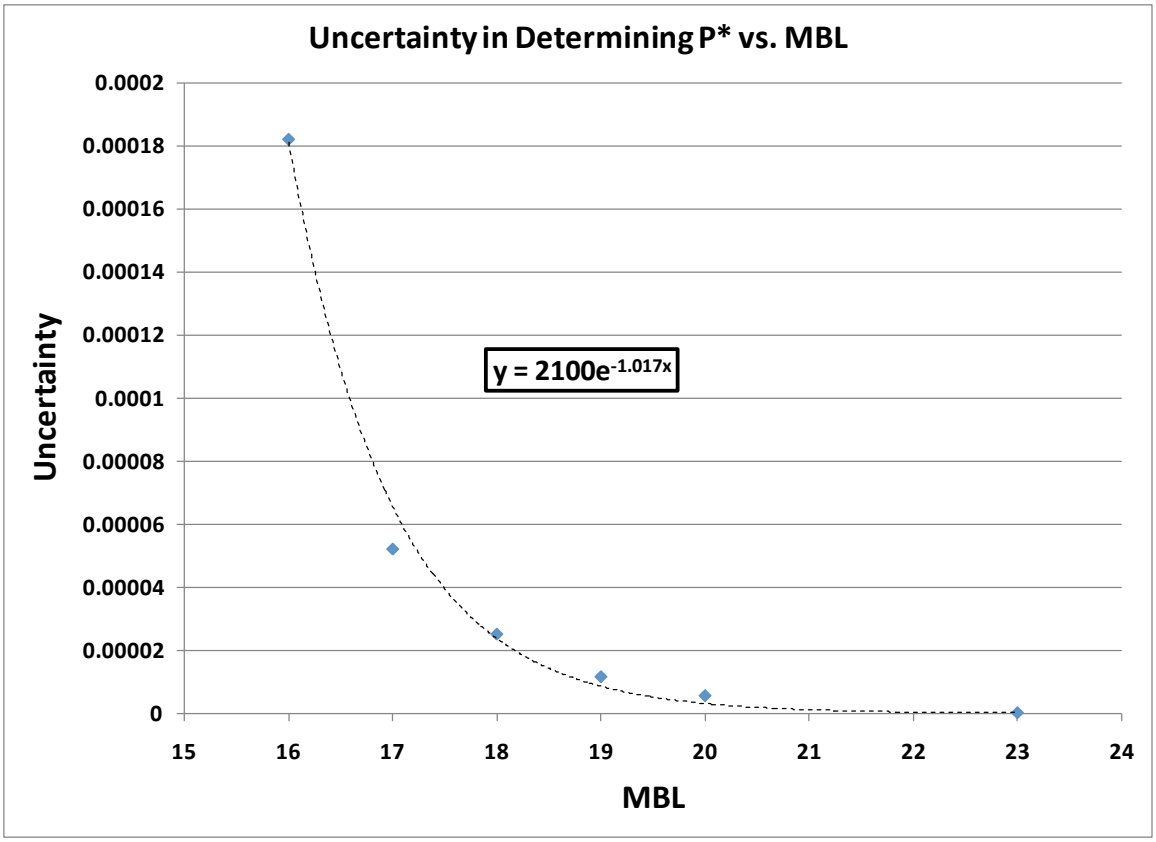

Figure 7: Uncertainty in estimating P* obtained by the simulation at different MBL values.

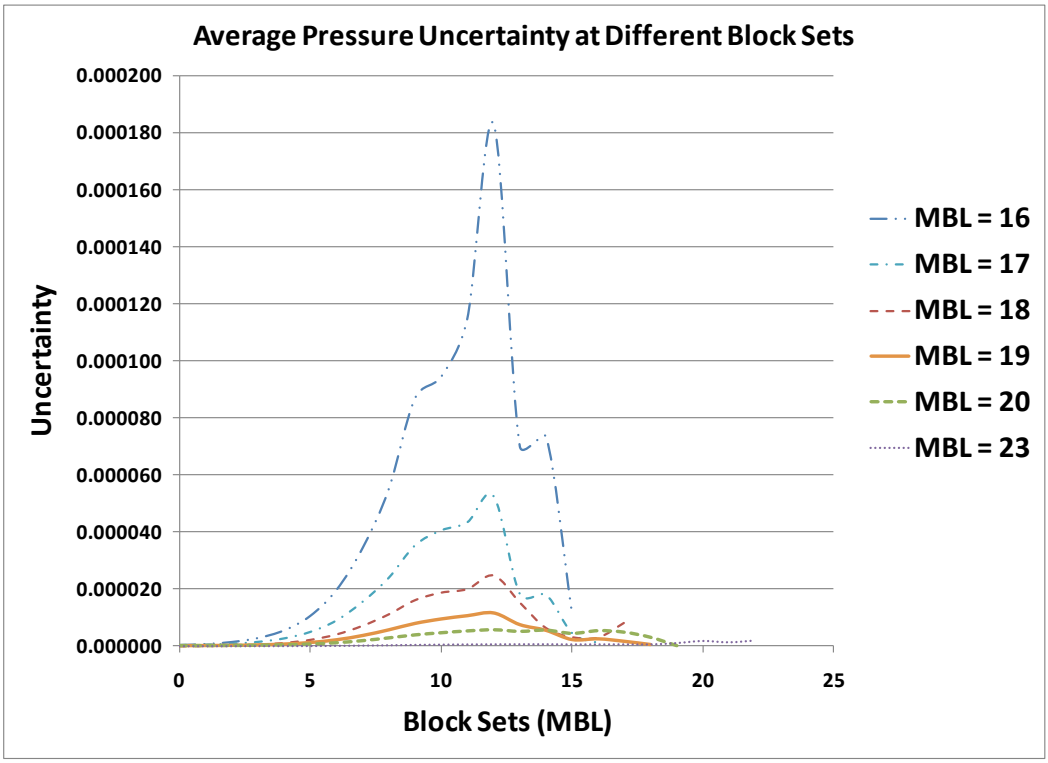

Figure 8: Uncertainty evolution plots with respect to block sets used and their convergence for iterations with different MBL values.

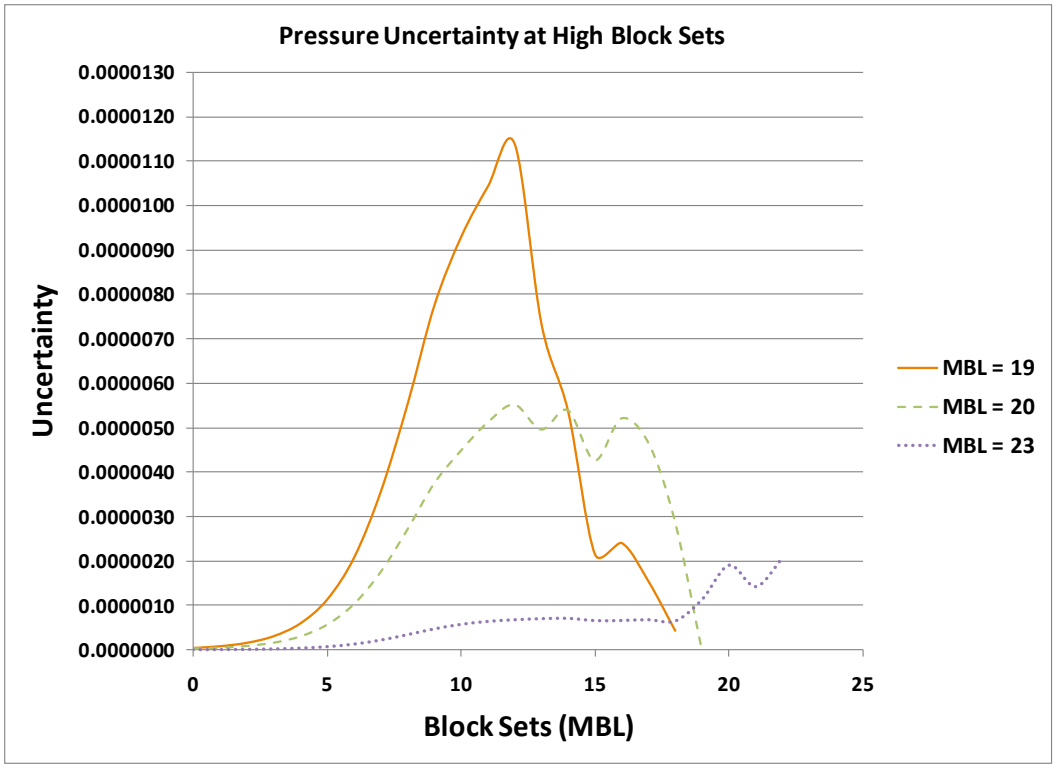

Figure 9: Uncertainty plots showing smoothness of convergence for high MBL iterations.

In this experimental set, another four experiments were conducted at T = 220 K at four different normalized densities for MBL = 20 iterations. As it was concluded from the second set of experiments the uncertainty increased with the increase of density (Figure 10) due to the increase in the fluctuations. This explains why at lower densities, such as 0.1175 and 0.3643, the errors were very small compared to the real data. However at higher densities the errors were more significant. Indeed, not only the model is blamed for the deviations from the correct real values but also the uncertainty in P* estimation.

As a closing remark for this set, the results obtained in second experimental set could be slightly improved (Figure 11) by increasing the number of iterations used to obtain P*. However for such progress to be achieved, the CPU time required is much higher compared to the original experiments conducted only at 20 million iterations.

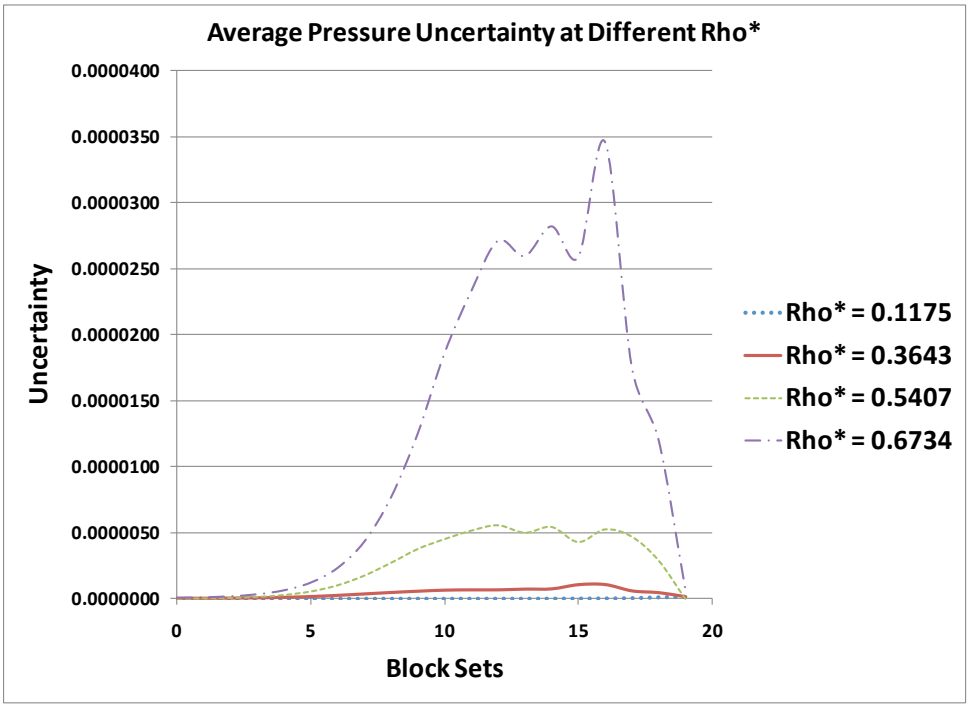

Figure 10: Evolution plots for average pressure uncertainty at different normalized densities at T = 220 K and MBL = 20.

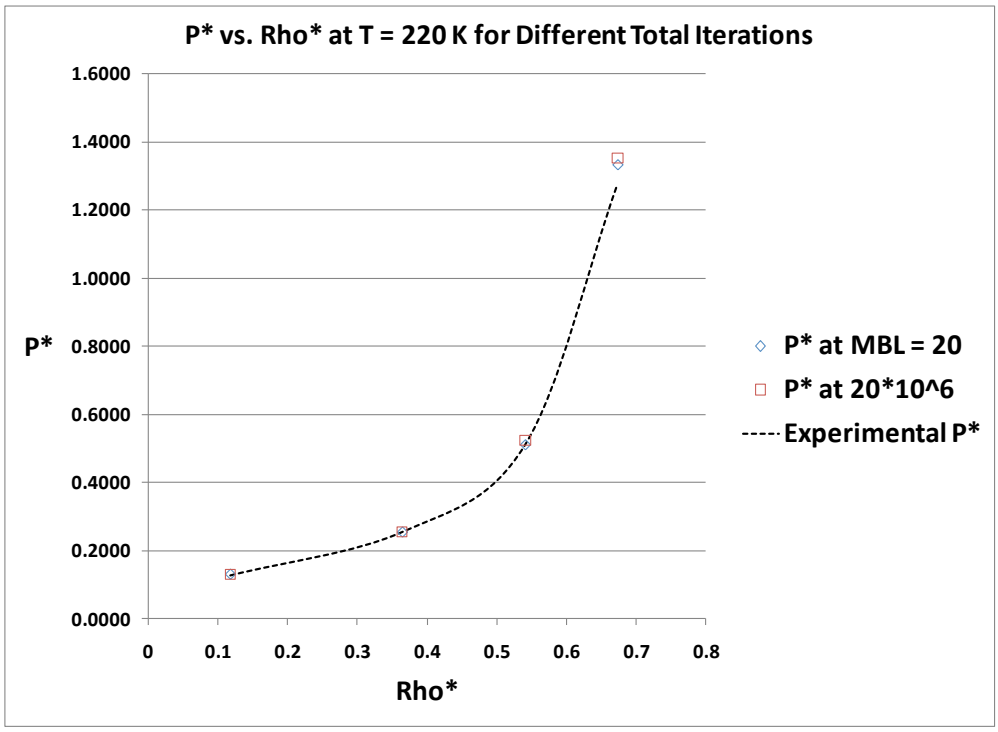

Figure 11: Comparison between P* obtained by MBL = 20 iterations and original P* obtained with 20 million iterations.

4. Experimental Set IV: Methane Isotherms above Critical Temperature Using Exp-6 Model in Canonical Ensemble

In this set, the same isotherms obtained by L-J model were reproduced using exp-6 potential model. Exp-6 provides more flexibility by having the dimensionless α (referred to as Alfa in plots and tables) parameter. At first a group of four experiments at T = 200 K and a range of different densities with four different α values (α = 14, 15, 16, and 17) were conducted in order to investigate the optimum value of α to be used. The estimated normalized pressure values (Figure 12), after 5 million iterations, increased as the value of α increased at same temperature and density. According to the results obtained, α was assigned to 15 as being the value that showed the best fit compared to others.

The same group of isotherms were reproduced by exp-6 model (T = 200, 220, 250, 300, and 400 K) with α = 15 at four different densities for each isotherm. P* values were estimated over 10 million iterations for each case. The values obtained were compared to the same experimental data (Figure 13) as in the L-J model set. Same observations regarding increase in error at higher densities and lower temperatures were detected. However, the agreement with the experimental data showed some small inconsistencies and was not good as in the L-J case. P* values obtained are tabulated (Appendix, Table IV.1) with their corresponding percentage errors.

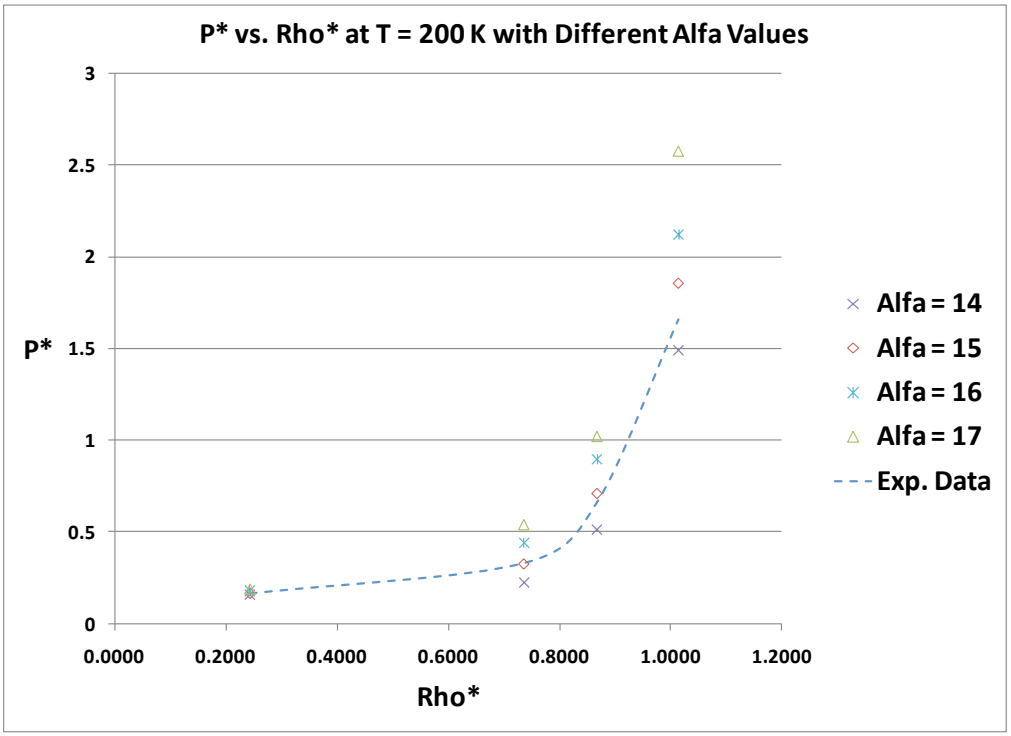

Figure 12: Normalized pressure evaluated by exp-6 model at different normalized densities at T = 200K for different α values (Symbols) compared to experimental data (Dashed line).

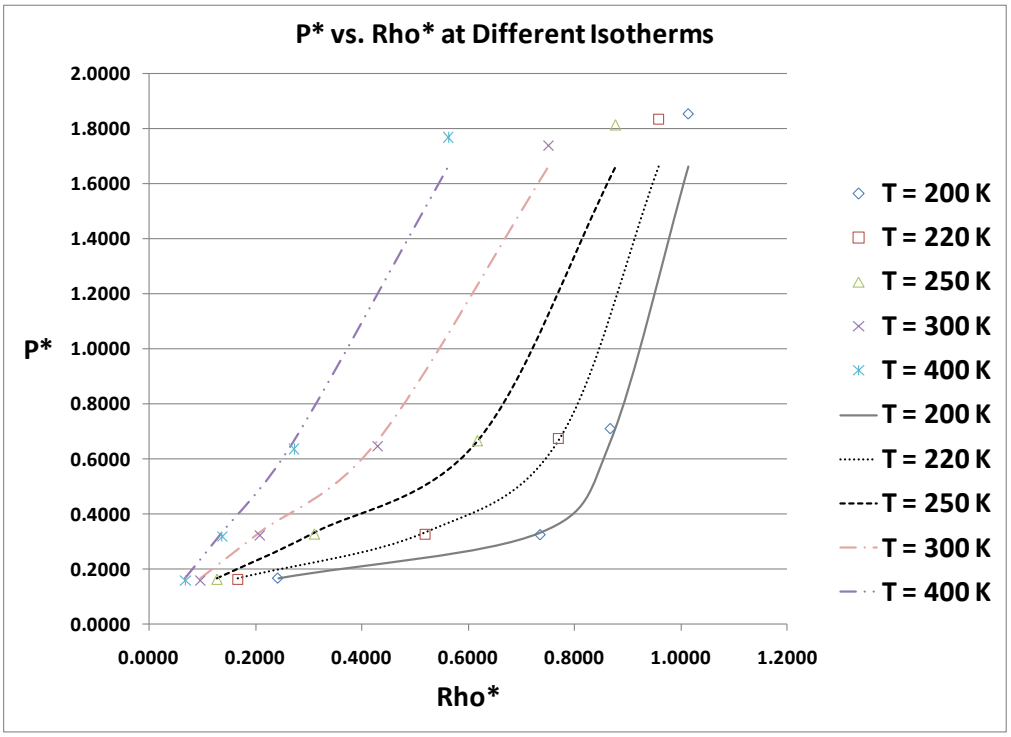

Figure 13: Normalized pressures obtained by exp-6 model with α = 15 (Symbols) compared to experimental isotherms plots (Lines).

Additional experiments were run with 10 million iterations using α = 14.5 for the highest density value at each isotherm expecting it to give better estimations than both L-J model and exp-6 at α = 15 model. The results at those densities were combined with the results obtained by L-J model at lower densities (Figure 14). The isotherms created by combining both models showed a very strong agreement with the data from literature, with higher accuracy achieved than each separately.

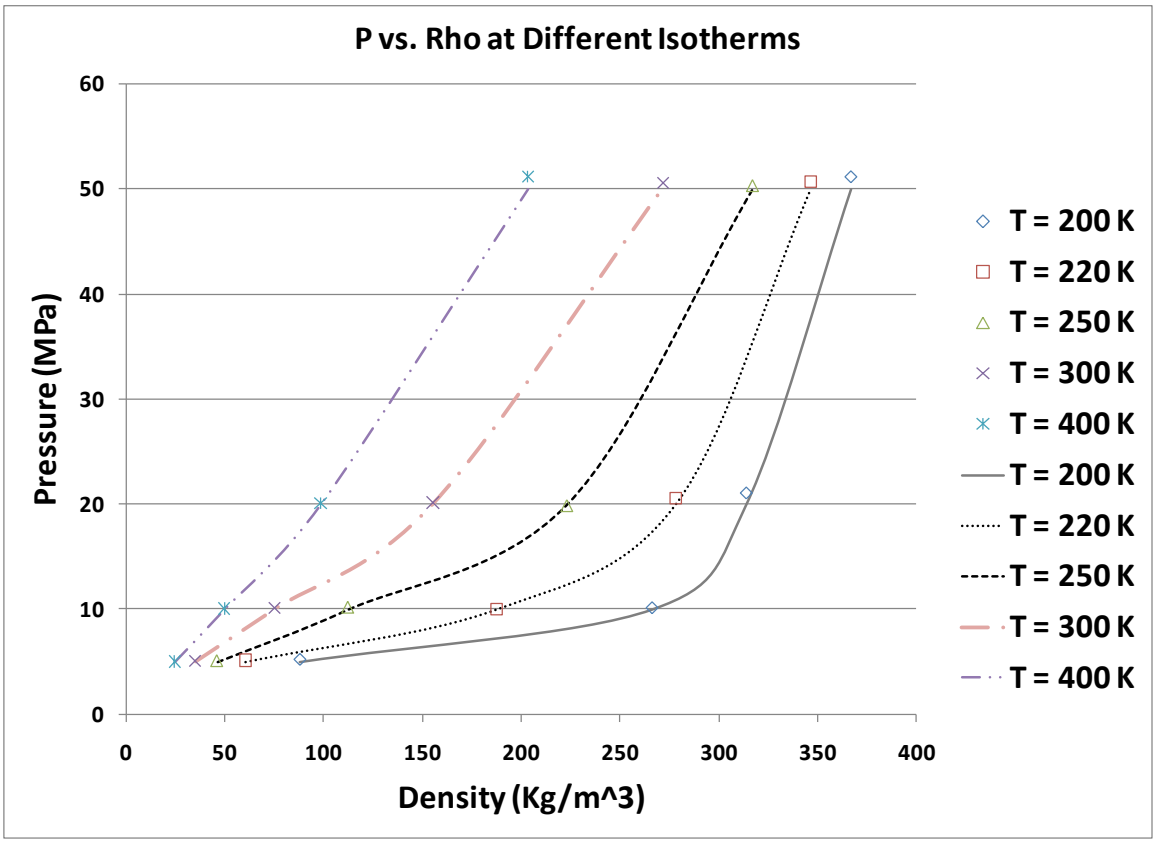

Figure 14: Isotherms estimated using both models (Symbols) compared to experimental data (Lines).

5. Experimental Set V: Methane Phase Behavior below Critical Temperature Using L-J Model in Gibbs Ensemble

To simulate the two phase behavior below critical temperature the Gibbs ensemble with two main boxes was used. Five experiments at temperatures below and near critical temperature (T_c* = 1.3 or T_c = 190.56 K) were done. The plots obtained by Gibbs code are different than the ones obtained by the canonical. For all experiments, the initial properties of the two main boxes were exact (N = 1000 and Rho* = 0.3). As the simulation proceeds, the densities recorded for each box split and converge (Appendix, Figures V.1-5) to two different values. It takes the simulation some time to judge which box to be assigned for the dense phase and which one for the lighter one.

In agreement with what have been concluded from the canonical experiments, the main box including the dense phase showed more fluctuations than the lighter one. Moreover, fluctuations increased in both boxes at higher temperatures; in other words, temperatures closer to the critical one.

The densities evaluated have been compared to the experimental data available. The normalized values and real ones for densities and temperatures are tabulated (Appendix, Table V.1) in addition to the percentage errors. Similar to the one phase case, the phase diagram predicted below critical temperature for methane (Figure 15) showed a good agreement with the experimental data. However, the deviations from the real data become more significant as we get closer to the critical temperature.

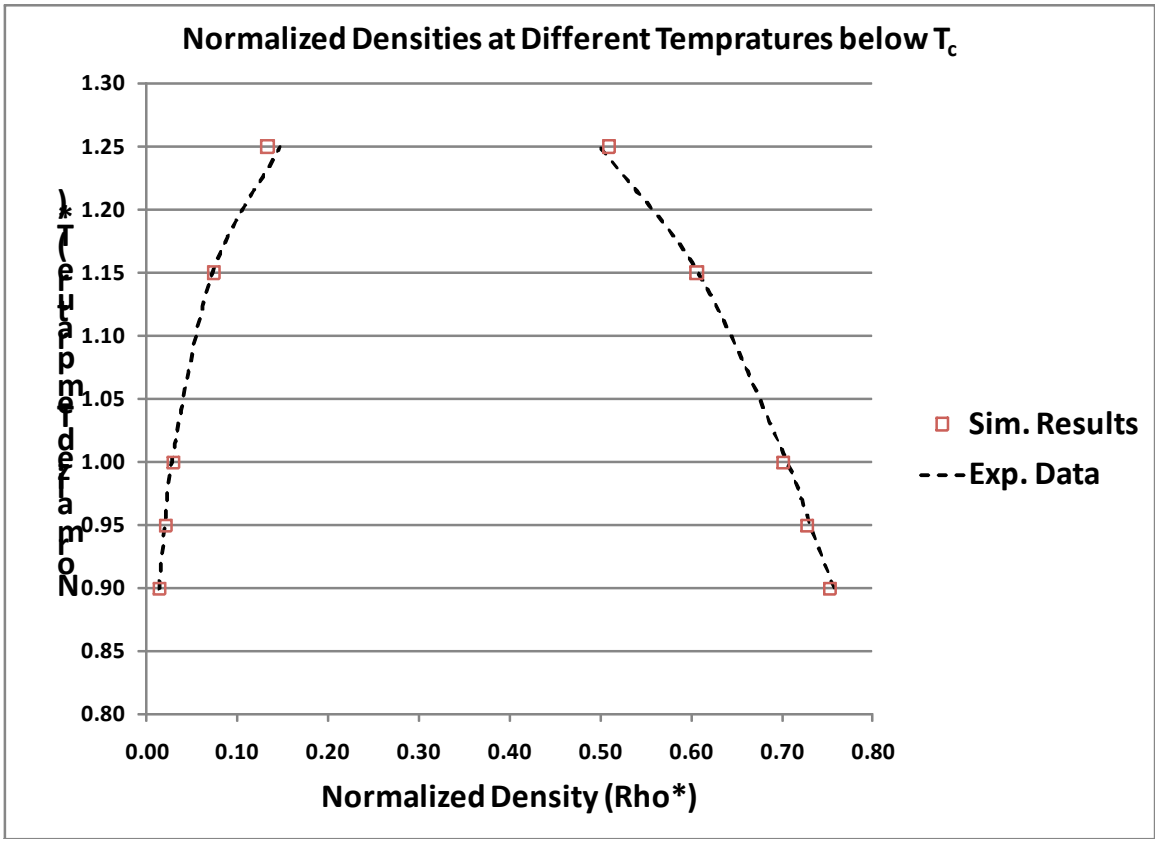

Figure 15: Methane phase diagram below critical temperature using L-J model in Gibbs ensemble (Symbols) compared to experimental diagram (Dashed line).

V- CONCLUSION

To sum up, a total of five experimental sets have been successfully conducted, reflecting how powerful and promising the MC simulation method is. Experiments can be categorized according to the ensemble and the potential model used in system's energy calculations. Simulations in canonical ensemble with L-J model and exp-6 were both successful in reproducing methane isotherms above critical temperature with a very high degree of accuracy. Accuracy was further enhanced by introducing the combination concept between both models, in which L-J was used in calculations at pressures lower than 25 MPa and exp-6 for higher pressures. Moreover, Gibbs ensemble coupled with L-J model was involved to construct methane two-phase envelope by running experiments at temperatures lower than the critical one.

The study was further enriched, by some statistical manipulations clarifying the uncertainty concept in estimating the average normalized pressure. In addition, parameters optimization experiments were performed to determine the best number of particles to mimic the real case with least running time possible; also α parameter existing in exp-6 model was optimized over a range of tested values.

In conclusion, results obtained showed an elegant fit compared to experimental data at all thermodynamic conditions investigated. To the best of our knowledge, a combination between models has never been used before, and indeed it proved to be beneficial.

VI- FUTURE WORK

Results have reflected the great potential in using molecular simulation methods. This potential is greatly beneficial in areas where real experiments at field are either difficult to conduct or even dangerous. As a near future project, MC simulations are to be applied in investigating the phase behavior of elemental sulfur in sour gases. Sulfur proved to be highly soluble in sour gases; however, at relaxed pressures and relatively low temperatures it may dissolute. Elemental sulfur dissolution may cause serious problems affecting the whole process of gas recovery. Therefore, highly accurate estimations for dissolution conditions help avoiding these troubles.

In real life applications, complexity increases as well as the approach dealing with. Therefore, in order to get more precise estimations the approach used in this study to predict phase behavior of methane is not enough, and some enhancements are required. Elemental sulfur possesses the longest list of allotropes after carbon; the most existing one is α-sulfur made of S_8 rings. Hence, using the point convention for representing methane molecules will not be well representative for the sulfur ones. As a result, intramolecular interactions including bonds bending, stretching and torsion are to be considered according to the models discussed earlier. Moreover, sulfur is an electronegative element and neglecting the polar interactions as have been assumed in the case of methane would not be a wise choice. For non-polar interactions, both intermolecular and intramolecular, using exp-6 with its flexibility term is more preferable; however, using L-J model is possible if it showed good precision.

BIBLIOGRAPHY

1. Latil, M., *Enhanced Oil Recovery*. 1980. p. 8-10.

2. Fanaritis, J. and G. Chilingarianeditor, *Chapter 7 Steam Enhanced Oil Recovery.* 1989. **19**: p. 221-282.

3. Stahl, C.R., et al., *Thermally Enhanced Oil Recovery Method and Apparatus*, U.S. Patent, Editor. 1987. p. 1-12.

4. Taylor, K.C. and H.A. Nasr-El-Din, *Water-soluble hydrophobically associating polymers for improved oil recovery* Journal of Petroleum Science and Engineering, 1998. **19**: p. 265-280.

5. Daripa, P. and G. Pasa, *An optimal viscosity profile in enhanced oil recovery by polymer flooding.* International Journal of Engineering Science, 2004. **42**(19-20): p. 2029-2039.

6. Iglauer, S., et al., *New surfactant classes for enhanced oil recovery and their tertiary oil recovery potential.* Journal of Petroleum Science and Engineering, 2010. **71**(1-2): p. 23-29.

7. Malloy, T.P. and R.J. Swedo, *Enhanced Oil Recovery*, U.S. Patent, Editor. 1985.

8. Soltanieh, M., A.M. Eslami, and A. Moradian, *Feasibility study of carbon dioxide capture from power plants and other major stationary sources and storage in Iranian oil fields for enhanced oil recovery (EOR).* Energy Procedia, 2009. **1**(1): p. 3663-3668.

9. Emery, L.W., *Enhanced Oil Recovery*, U.S. Patents, Editor. 1985.

10. Todd, M.R. and G.W. Grand, *Enhanced Oil Recovery Using Carbon Dioxide.* Energy Conversion and Management, 1993. **34**(9-11): p. 1157-1164.

11. Herzog, H. and D. Golomb, *Carbon Capture and Storage from fossil fuel to storge.* Encyclopedia of Energy, 2004. **1**: p. 1-11.

12. Bryant, E., *Climate Process and Change*, in *Cambridge University Press*. 1997. p. 209.

13. Bachu, S. and J.J. Adams, *Sequestration of CO_2 in geological media in response to climate change: capacity of deep saline aquifers to sequester CO_2 in solution.* Energy Conversion and Management, 2003. **44**(20): p. 3151-3175.

14. Gaspar Ravagnani, A.T.F.S., E.L. Ligero, and S.B. Suslick, *CO_2 sequestration through enhanced oil recovery in a mature oil field.* Journal of Petroleum Science and Engineering, 2009. **65**(3-4): p. 129-138.

15. Leach, A., C.F. Mason, and K.v.t. Veld, *Co-optimization of enhanced oil recovery and carbon sequestration.* Resource and Energy Economics, 2011.

16. Worden, R.H. and P.C. Smalley, *H_2S-producing reactions in deep carbonate gas reservoirs: Khuff Formation, Abu Dhabi.* Chemical Geology 1996. **133**: p. 157-171.

17. Cézac, P., et al., *Elemental sulphur deposition in natural gas transmission and distribution networks.* The Journal of Supercritical Fluids, 2008. **44**: p. 115-122.

18. Chesnoy, A.-B. and D.J. Pack, *S8 threatens natural gas operations, enviornment.* Oil and Gas Journal 1997. **95**(17): p. 74-78.

19. Wilkes, C. and V. Pareek, *Sulfur deposition in a gas turbine natural gas fuel control system.* Energy-Tech Online, 2001.

20. Pack, D.J., *Elemental sulphur formation in natural gas transmission pipelines* in *14th Biennal Joint Technical Meeting on Pipelines Research* 2003: Berlin, Germany. p. 1-14.

21. Abou-Kassem, J.H., *Experimental and numerical modeling of sulfur plugging in carbonate reservoirs.* Journal of Petroleum Science and Engineering, 2000. **26**: p. 91-103.

22. Roberts, B.E., *The effect of Sulfur deposition on gaswell inflow performance.* SPE Reservoir Engineering, 1997: p. 118-123.

23. Kennedy, H.T. and D.R. Wieland, *Equilibrium in the methane-carbon dioxide-hydrogen sulfide-sulfur system* Petroleum Transcations, AIME, 1960. **219**: p. 166-169.

24. Roof, J.G., *Solubility of sulfur in hydrogen sulfide and in carbon disulfide at elevated temperature and pressure.* Society of Petroleum Engineers Journal, 1971: p. 272-276.

25. Swift, S.C., F.S. Manning, and R.E. Thompson, *Sulfur-bearing capacity of hydrogen sulfide gas.* Society of Petroleum Engineers Journal, 1976: p. 57-64.

26. Brunner, E. and W.H. Woll, *Solubility of sulfur in hydrogen sulfide and sour gas.* Society of Petroleum Engineers Journal 1980: p. 377-384.

27. Gu, M., et al., *Experimental and modeling studies on the phase behavior of high H_2S-content natural gas mixtures.* Fluid Phase Equilibria, 1993. **82**: p. 173-182.

28. Migdisov, A.A., O.M. Suleimenov, and Y.V. Alekhin, *Experimental study of polysulfane stability in gaseous hydrogen sulfide.* Geochimica et Cosmochimica Acta, 1998. **62**(15): p. 2627-2635.

29. Brunner, E., M.C. Place, and W.H. Woll, *Sulfur solubility in sour gas.* Journal of Petroleum Technology, 1988: p. 1587-1592.

30. Davis, P.M., C.S.C. Lau, and J.B. Hyne, *Data on the solubility of sulfur in sour gases.* Alberta Sulfur Research Ltd., 1992. **93**(XXIX): p. 1.

31. Chen, C.-Y. and G.-J. Sun, *Experimental and modeling studies on the phase behavior of high H_2S-content natural gas mixtures.* Fluid Phase Equilibria, 2003. **82**: p. 173-182.

32. Kendall, J. and J.C. Andrews, *The solubilities of acids in aqueous solutions of other acids.* Journal of American Chemical Society, 1921. **43**: p. 1545-1560.

33. Selleck, F.T., L.T. Carmichael, and B.H. Sage, *Phase behavior in the hydrogen sulfide-water system.* Industrial and Engineering Chemistry, 1952. **44**(9): p. 2219-2226.

34. Clarke, E.C.W. and N. Glew, *Aqueous nonelectrolyte solutions. Part VIII. deuterium and hydrogen sulfides solubilities in deuterium oxide and water.* Canadian Journal of Chemistry, 1971. **49**: p. 691-698.

35. Gerrard, W., *Solubility of hydrogen sulphide, dimethyl ether, methyl chloride and sulphur dioxide in liquids. The prediction of solubility of all gases.* Journal of Applied Chemistry and Biotechnology, 1972. **22**: p. 623-650.

36. Douabul, A.A. and J.P. Riley, *The solubility of gases in distilled water and seawater-V. Hydrogen sulphide.* Deep-Sea Research, 1979. **26A**: p. 259-268.

37. Dohrn, R. and G. Brunner, *High-pressure fluid-phase equilibria: experimental methods and systems investigated (1988-1993).* Fluid Phase Equilibria, 1995. **106**: p. 213-282.

38. Subra, P., et al., *Contribution to the determination of the solubility of beta-carotene in supercritical carbob dioxide and nitrous oxide: experimental data and modeling.* Fluid Phase Equilibria, 1997. **131**: p. 269-286.

39. Murga, R., et al., *Solubility of three hydroxycinnamic acids in supercritical carbon dioxide.* The Journal of Supercritical Fluids, 2003. **27**(3): p. 239-245.

40. Coimbra, P., et al., *Experimental determination and correlation of Artemisinin's solubility in supercritical carbon dioxide.* Journal of Chemical and Engineering Data, 2006. **51**: p. 1097-1104.

41. Chrastil, J., *Solubility of solids and liquids in supercritical gases.* Journal of Physical Chemstry 1982. **86**: p. 3016-3021.

42. Valle, J.M.d. and J.M. Aguilera, *An improved equation for predicting the solubility of vegetable oils in supercritical CO_2.* Industrial and Engineering Chemistry Research, 1988. **27**: p. 1553-1555.

43. Kumar, S.K. and K.P. Johnston, *Modelling the solubility of solids in supercritical fluids with density as the independent variable.* The Journal of Supercritical Fluids, 1988. **1**: p. 15-22.

44. Mendez-Santiago, J. and A.S. Teja, *The solubility of solids in supercritical fluids.* Fluid Phase Equilibria, 1999. **158-160**: p. 501-510.

45. Bartle, K.D., A.A. Clifford, and S.A. Jafar, *Measurement of solubility in supercritical fluids using chromatographic retention: the solubility of fluorene, phenanthrene, and pyrene in carbon dioxide.* Journal of Chemical and Engineering Data, 1990. **35**: p. 355-360.

46. Vafajoo, L., M. Mirzajanzadeh, and F. Zabihi, *Determining correlations for prediction of the solubility behavior of ibuprofen in supercritical carbon dioxide utilizing density based models.* World Academy of Science, Engineering and Technology, 2011. **73**: p. 790-792.

47. Lucas, A.d., et al., *Solubility determination and model prediction of oilve husk oil in supercritical carbon dioxide and cosolvents.* Industrial and Engineering Chemistry Research 2007. **46**: p. 5061-5066.

48. Skerget, M., Z. Knez, and M. Habulin, *Solubility of beta-carotene and oleic acid in dense CO_2 and data correlation by a density based model* Fluid Phase Equilibria, 1995. **109**: p. 131-138.

49. Li, S., G.S. Varadarajan, and S. Hartland, *Solubilities of theobromine and caffeine in supercritical carbon dioxide: correlation with density-based models* Fluid Phase Equilibria, 1991. **68**: p. 263-280.

50. Carroll, J.J., *Solubility of sulfur in sour gas mixtures.* Gas Liquids Engineering, 2009: p. 267-285.

51. Waals, J.D., *On the continuity of the gas and liquid state* 1873, Leiden.

52. Karan, K., R.A. Heidemann, and L.A. Behie, *Sulfur solubility in sour gas: predictions with an equation of state model.* Industrial and Engineering Chemistry Research, 1998. **37**: p. 1679-1684.

53. Soave, G., *Equilibrium constants from a modified Redlich-Kwong equation of state.* Chemical Engineering Science, 1972. **27**: p. 1197-1203.

54. Peng, D. and D.B. Robinson, *A new two-constant equation of state.* Industrial and Engineering Chemistry Fundamentals, 1974. **15**(1): p. 59-64.

55. Berro, C., L. Barna, and E. Rauzy, *A group-contribution equation of state for predicting vapor-liquid equilibria and volumetric properties of carbon dioxide-hydrocarbons systems.* Fluid Phase Equilibria, 1996. **114**: p. 63-87.

56. Tsai, J. and Y. Chen, *Application of a volume-translated Peng-Robinson equation of state on vapor-liquid equilibrium calculations.* Fluid Phase Equilibria, 1998. **145**: p. 193-215.

57. Harismiadis, V.I., A.Z. Panagiotopoulos, and D.P. Tassios, *Phase equilibria of binary Lennard-Jones mixtures with cubic equations of state.* Fluid Phase Equilibria, 1994. **94**: p. 1-18.

58. Salerno, S., et al., *Prediction of vapor pressures and saturated volumes with a simple cubic equation of state: Part I: A reliable data base.* Fluid Phase Equilibria, 1986. **27**: p. 15-34.

59. Twu, C.H., et al., *A cubic equation of state with a new alpha function and a new mixing rule.* Fluid Phase Equilibria, 1991. **69**: p. 33-50.

60. Tomcej, R.A., H. Kalra, and B.E. Hunter, *Prediction of sulphur solubility in sour gas mixtures*, in *39th Annual Technical Meeting of the Petroleum Society of CIM*. 1988: Calgary, Alberta.

61. Heidemann, R.A., et al., *A chemical equilibrium equation of state model for elemental*

sulfur and sulfur-containing fluids. Industrial and Engineering Chemistry Research, 2001. **40**: p. 2160-2167.

62. Folas, G.K., et al., *Recent applications of the cubic-plus-association (CPA) equation of state to industrially important systems.* Fluid Phase Equilibria, 2005. **228-229**: p. 121-126.

63. Folas, G.K., et al., *Vapor–liquid, liquid–liquid and vapor–liquid–liquid equilibrium of binary and multicomponent systems with MEGModeling with the CPA EoS and an EoS/GE model.* Fluid Phase Equilibria, 2006. **249**(1-2): p. 67-74.

64. Kontogeorgis, G.M., et al., *Modelling of associating mixtures for applications in the oil & gas and chemical industries.* Fluid Phase Equilibria, 2007. **261**: p. 205-211.

65. Folas, G., et al., *High-pressure vapor–liquid equilibria of systems containing ethylene glycol, water and methaneExperimental measurements and modeling.* Fluid Phase Equilibria, 2007. **251**(1): p. 52-58.

66. Escobedo-Alvarado, G.N., S.I. Sandler, and A.M. Scurto, *Modeling of solid-supercritical fluid phase equilibria with a cubic equation of state- G^{ex} model* Journal of Supercritical Fluids, 2001. **21**: p. 123-134.

67. Voutsas, E., et al., *Vapor liquid equilibrium modeling of alkane systems with Equations of State: "Simplicity versus complexity".* Fluid Phase Equilibria, 2006. **240**: p. 127-139.

68. Kraska, T. and K.E. Gubbins, *Phase equilibria calculations with a modified SAFT equation of state. 2. Binary mixtures of n-alkanes, 1-alkanols, and water* Industrial and Engineering Chemistry Research, 1996. **35**: p. 4738-4746.

69. Kahl, H. and S. Enders, *Calculation of surface properties of pure fluids using density gradient theory and SAFT-EOS.* Fluid Phase Equilibria, 2000. **172**: p. 27-42.

70. Ikonomou, G.D. and M.D. Donohue, *Thermodynamics of hydrogen-bonded molecules: The associated perturbed anisotropic chain theory.* AIChE Journal, 1986. **32**(10): p. 1716-1725.

71. Economou, I.G. and M.D. Donohue, *Equation of state with multiple associating sites for water and water-hydrocarbon mixtures.* Industrial and Engineering Chemistry Research, 1992. **31**: p. 2388-2394.

72. Panayiotou, C., et al., *Nonrandom hydrogen-bonding model of fluids and their mixtures. 1. Pure fluids* industrial and Engineering Chemistry Research, 2004. **43**: p. 6592-6606.

73. Panayiotou, C., I. Tsivintzelis, and I.G. Economou, *Nonrandom hydrogen-bonding model of fluids and their mixtures. 2. Multicomponent mixtures.* industrial and Engineering Chemistry Research, 2007. **46**: p. 2628-2636.

74. Sanchez, I.C. and R.H. Lacombe, *An elementary molecular theory of classical fluids. Pure fluids.* Journal of Physical Chemistry, 1976. **80**(21): p. 2352-2362.

75. Chapman, W.G., et al., *New reference equation of state for associating liquids.* industrial and Engineering Chemistry Research, 1990. **29**: p. 1709-1721.

76. Huang, S.H. and M. Radosz, *Equation of state for small, large, polydisperse, and associating molecules.* industrial and Engineering Chemistry Research 1990. **29**: p. 2284-2294.

77. Blas, F.J. and L.F. Vega, *Prediction of binary and ternary diagrams using the statistical associating fluid theory (SAFT) equation of state.* industrial and Engineering Chemistry Research, 1998. **37**: p. 660-674.

78. Karakatsani, E.K., T. Spyriouni, and I.G. Economou, *Extended statistical asociating fluid theory (SAFT) equations of state for dipolar fluids.* AIChE Journal, 2005. **51**(8): p. 2328-2342.

79. Galindo, A., et al., *SAFT-VRE: Phase behavior of electrolyte solutions with the statistical associating fluid theory for potentails of variable range* Journal of Physical Chemistry B, 1999. **103**: p. 10272-10281.

80. Economou, I.G., *Statistical Associating fluid theory: A successful model for the calculation of thermodynamic and phase equilibrium properties complex fluid mixtures* industrial and Engineering Chemistry Research, 2002. **41**: p. 953-962.

81. Frenkel, D. and B. Smit, *Understanding molecular simulation: From algorithms to applications*. 2nd ed. Computational Science Series. Vol. 1. 1996: Academic Press.

82. Ungerer, P., et al., *Molecular simulation of the thermophysical properties of fluids: From understanding toward quantitative predictions.* Journal of Molecular Liquids, 2007. **134**(1-3): p. 71-89.

83. Panagiotopoulos, A.Z., *Direct determination of phase coexistence properties of fluids by Monte Carlo simulation in a new ensemble.* Molecular Physics, 1987. **61**(4): p. 813-826.

84. Lennard-Jones, J.E. and W.R. Cook, *The molecular fields of hydrogen, nitrogen and neon.* Proceedings of the Royal Society A: Mathematical, Physical and Engineering Sciences, 1926. **112**(760): p. 214-229.

85. Buckingham, R.A., *The classical equation of state of gaseous helium, neon and argon.* The Royal Society, 1938: p. 264-283.

86. Ungerer, P., V. Lachet, and B. Tavitian, *Applications of molecular simulation in oil and gas production and processing.* Oil and Gas Science and Technology-Reviews, 2006. **61**(3): p. 387-403.

87. Panagiotopoulos, A.Z., *Exact calculations of fluid-phase equilibria by Monte Carlo simulation in a new statistical ensemble.* International Journal of Thermophysics, 1989. **10**(2): p. 447-457.

88. Errington, J.R. and A.Z. Panagiotopoulos, *A fixed point charge model for water optimized to the vapor-liquid coexistence properties.* Journal of physical Chemistry B, 1998. **102**: p. 7470-7475.

89. Errington, J.R. and A.Z. Panagiotopoulos, *A new intermolecular potential model for the n-Alkane homologous series.* Journal of physical Chemistry B, 1999. **103**: p. 6314-6322.

90. Panagiotopoulos, A.Z., *Molecular simulation of phase coexistence: Finite-size effects and determination of critical parameters for*

two- and three-dimensional Lennard-Jones fluids. International Journal of Thermophysics, 1994. **15**(6): p. 1057-1072.

91. Panagiotopoulos, A.Z., et al., *Phase equilibria by simulation in the Gibbs ensemble: Alternative derivation, generalization and application to mixture and membrane equilibria.* Molecular Physics, 1988. **63**(4): p. 527-545.

92. Panagiotopoulos, A.Z., *Adsorption and capillary condensation of fluids in cylindrical pores by Monte Carlo simulation in the Gibbs ensemble.* Molecular Physics, 1987. **62**(3): p. 701-719.

93. Potoff, J.J., J.R. Errington, and A.Z. Panagiotopoulos, *Molecular simulation of phase equilibria for mixtures of polar and non-polar components.* Molecular Physics, 1999. **97**(10): p. 1073-1083.

94. Panagiotopoulos, A.Z., *Molecular simulation of phase equilibria: simple, ionic and polymeric fluids.* Fluid Phase Equilibria, 1992. **76**: p. 97-112.

95. Errington, J.R., et al., *molecular simulation of phase equilibria for water-methane and water-ethane mixtures.* Journal of physical Chemistry B, 1998. **102**: p. 8865-8873.

96. Vorholdz, J., et al., *Vapor+liquid equilibrium of water+carbon dioxide, and the binary system, waterqcarbon dioxide, from molecular simulation.* Fluid Phase Equilibria, 2000. **170**: p. 203-234.

97. Gunsteren, W.E.v. and H.J.C. Berendsen, *Computer simulation of molecular dynamics: Methodology, applications, and perspectives in chemistry.* Angewandte Chemie International Edition English, 1990. **29**: p. 992-1023.

98. Brunger, A.T., J. Kuriyan, and M. Karplus, *Crystallographic R factor refinement by molecular dynamics.* Science, 1987. **235**: p. 458-460.

99. Tully, J.C., *Molecular dynamics with electronic transitions.* Journal of Physical Chemistry, 1990. **93**(2): p. 1061-1071.

100. Leasure, S.C., K.F. Milfeld, and R.E. Wyatt, *Quantum molecular dynamics in intense laser fields: Theory and applications to diatomic molecules.* Journal of Physical Chemistry, 1981. **74**(11): p. 6197-6211.

101. Karplus, M. and J.A. McCammon, *Molecular dynamics simualtions of biomolecules.* Nature Structural Biology, 2002. **9**(9): p. 646-652.

102. Martin, M.G. and J.I. Siepmann, *Transferable potentials for phase equilibria. 1. United-Atom description of n-alkanes.* Journal of physical Chemistry B, 1998. **102**(14): p. 2569-2577.

103. Errington, J.R. and A.Z. Panagiotopoulosa, *Phase equilibria of the modified Buckingham exponential-6 potential from Hamiltonian scaling grand canonical Monte Carlo.* Journal of Chemical Physics, 1998. **109**(3): p. 1903-1100.

104. Setzmann, U. and W. Wagner, *A new equation of state and tables of thermodynamic properties for methane covering the range from melting line to 625 K at pressures up to 1000 MPa.* Journal of Physical Chemistry, 1991. **20**(6): p. 1061-1155.

105. Flyvbjerg, H. and H.G. Petersen, *Error estimates on averages of correlated data.* Journal of Chemical Physics, 1989. **91**(1): p. 461-466.

APPENDIX

Experimental Set I:

Figures I.1-10: Experiments with different number of particles (N) ranging from 100 to 1000 at T = 220 K and normalized density of 0.5407 using L-J potential model in canonical ensemble with 10 million iteration.

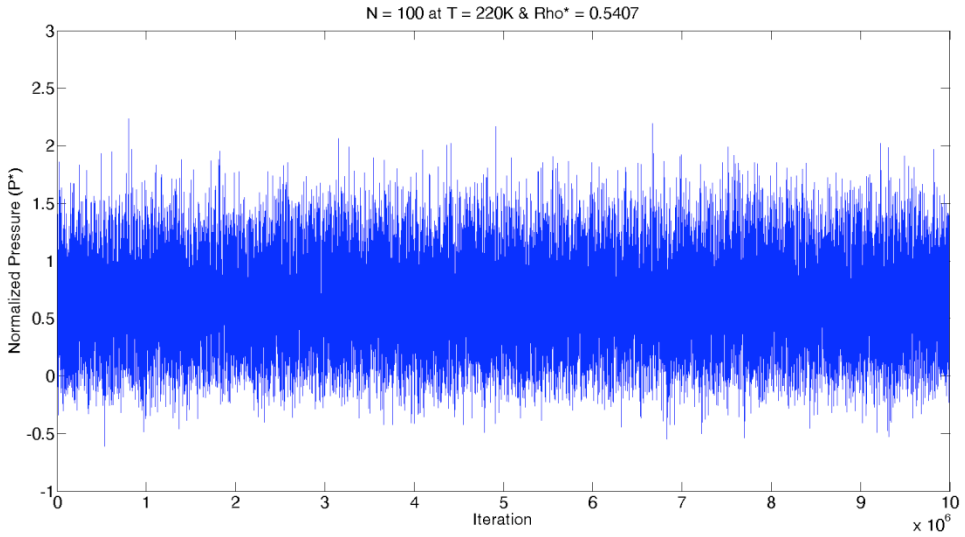

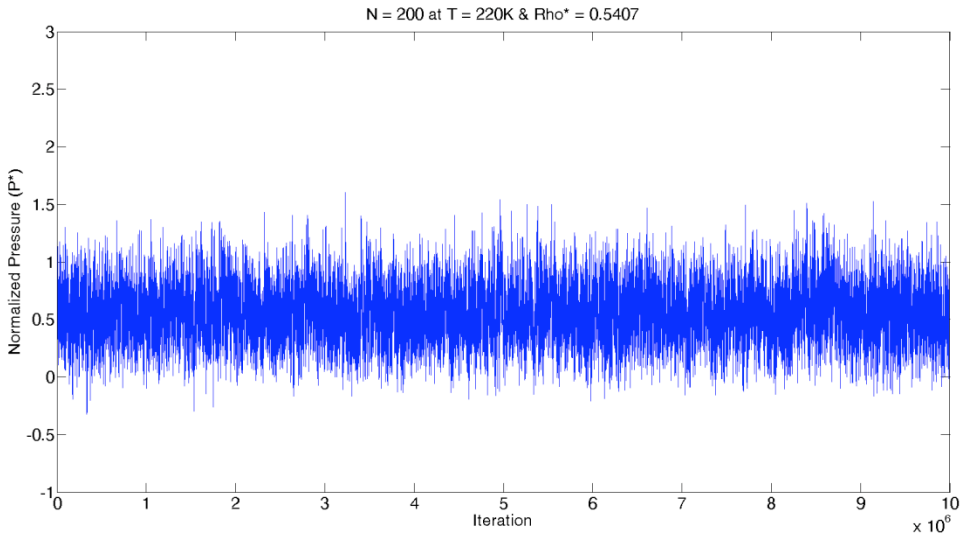

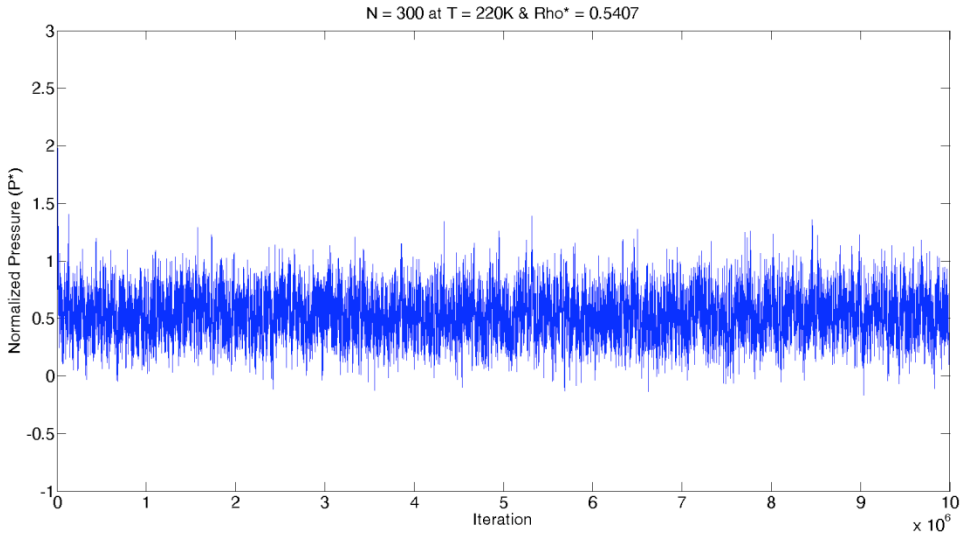
N = 300 at T = 220K & Rho* = 0.5407
Normalized Pressure (P*)
Iteration
x 10^6

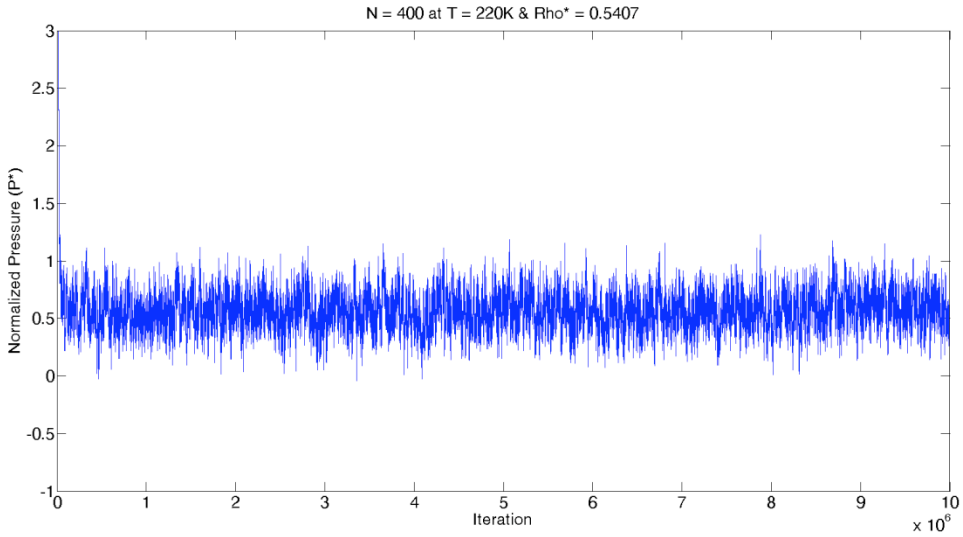
N = 400 at T = 220K & Rho* = 0.5407
Normalized Pressure (P*)
Iteration
x 10^6

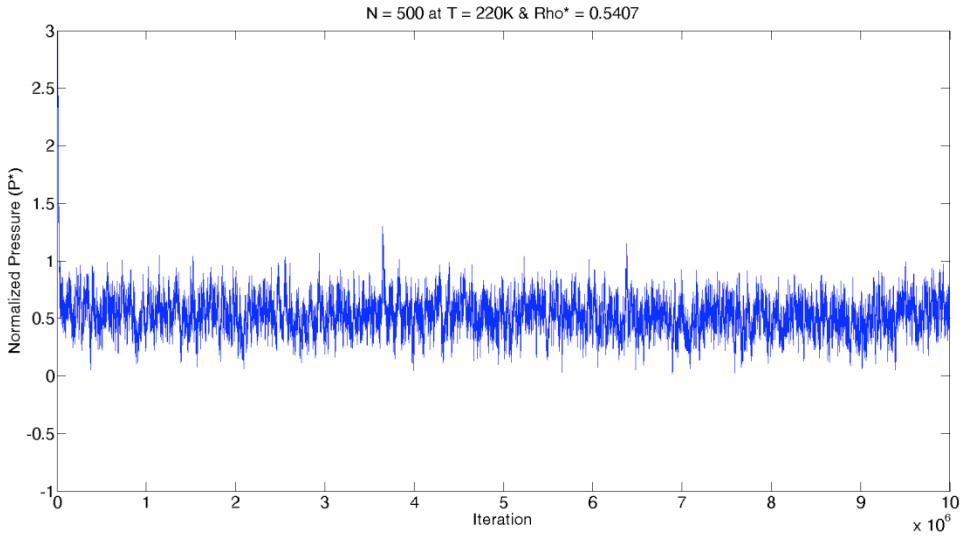
N = 500 at T = 220K & Rho* = 0.5407
Normalized Pressure (P*)
Iteration
x 10^6

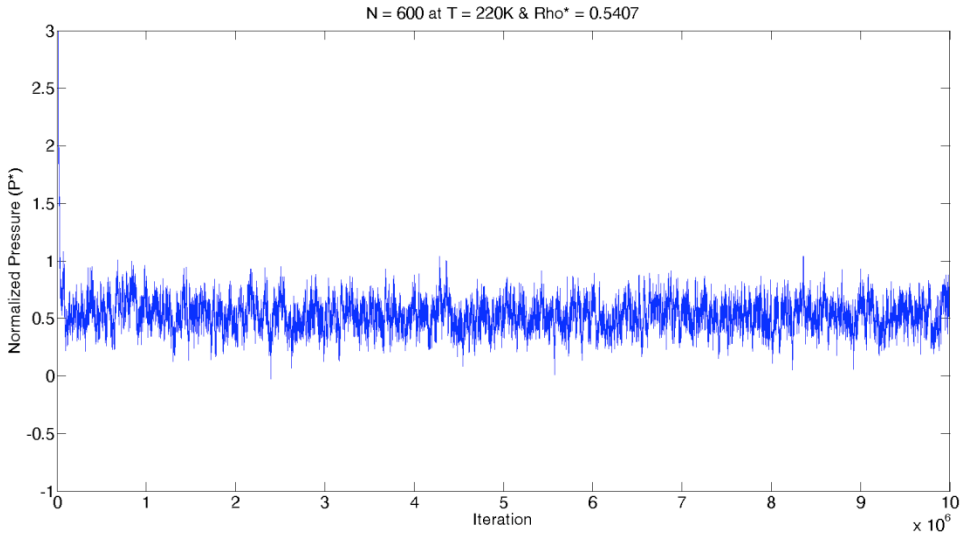
N = 600 at T = 220K & Rho* = 0.5407
Normalized Pressure (P*)
Iteration
x 10^6

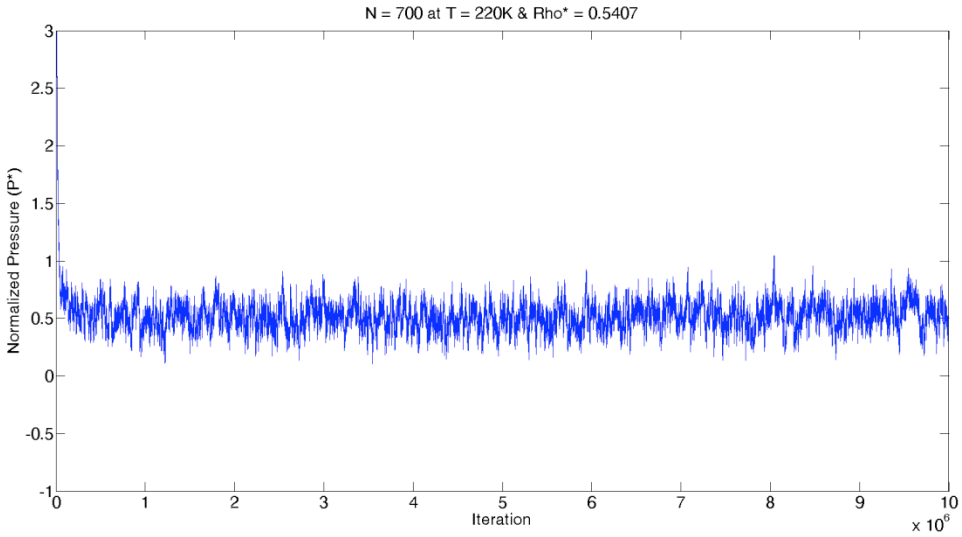
N = 700 at T = 220K & Rho* = 0.5407
Normalized Pressure (P*)
Iteration
x 10^6

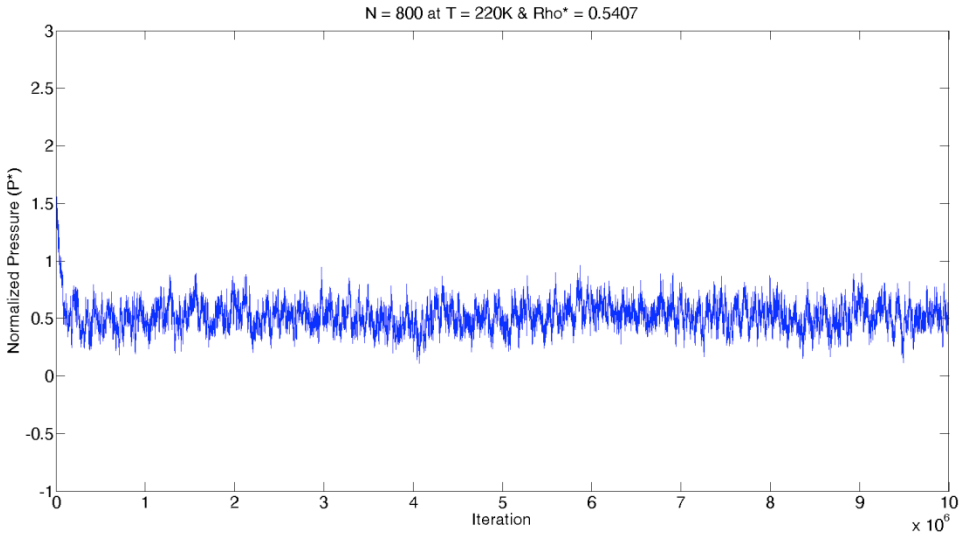
N = 800 at T = 220K & Rho* = 0.5407
Normalized Pressure (P*)
Iteration
x 10^6

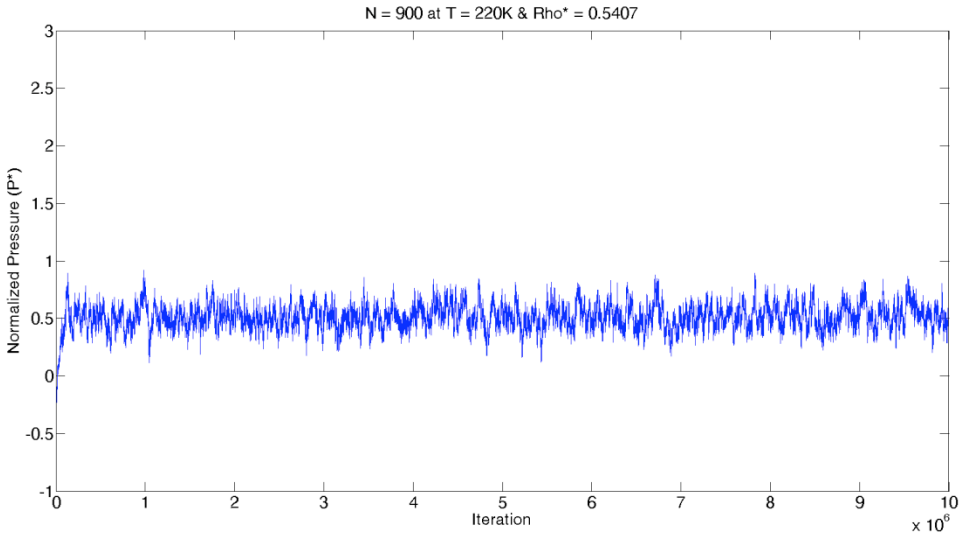
N = 900 at T = 220K & Rho* = 0.5407
Normalized Pressure (P*)
Iteration
x 10^6

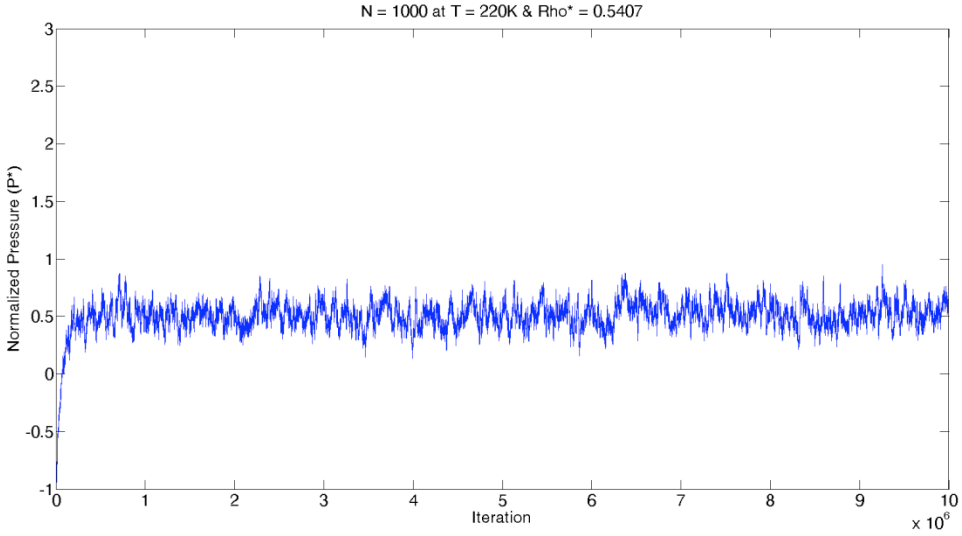
N = 1000 at T = 220K & Rho* = 0.5407
Normalized Pressure (P*)
Iteration
x 10^6

Experimental Set II:

Table II.1: Summary of data obtained (Appendix, Figures II.1-5) using L-J model at different densities and temperature combinations above critical temperature of methane. Collected data is compared to the experimental data obtained by Setzmann and Wagner [104].

Temperature	Density		Simulation Results		Experimental Data		
	Density	Normalized Density	Normalized Pressure	Pressure	Normalized Pressure	Pressure	Error
For T = 200 K							
	Rho (Kg/m^3)	**Rho***	**P***	**P(MPa)**	**P***	**P (MPa)**	**%**
	87.7640	0.1705	0.1322	5.1970	0.1272	5.0000	3.9391
	266.1900	0.5170	0.2572	10.1109	0.2544	10.0000	1.1086
	313.9100	0.6097	0.5351	21.0355	0.5088	20.0000	5.1774
	366.9200	0.7126	1.3652	53.6678	1.2719	50.0000	7.3356
For T = 220 K							
	Rho (Kg/m^3)	**Rho***	**P***	**P(MPa)**	**P***	**P (MPa)**	**%**
	60.4790	0.1175	0.1302	5.1183	0.1272	5.0000	2.3666
	187.5900	0.3643	0.2540	9.9851	0.2544	10.0000	0.1493
	278.3700	0.5407	0.5234	20.5755	0.5088	20.0000	2.8776
	346.7400	0.6734	1.3517	53.1371	1.2719	50.0000	6.2741
For T = 250 K							
	Rho (Kg/m^3)	**Rho***	**P***	**P(MPa)**	**P***	**P (MPa)**	**%**
	46.1590	0.0897	0.1289	5.0672	0.1272	5.0000	1.3445
	112.4300	0.2184	0.2585	10.1620	0.2544	10.0000	1.6197
	223.2300	0.4336	0.5046	19.8365	0.5088	20.0000	0.8176
	317.1500	0.6160	1.3076	51.4034	1.2719	50.0000	2.8069
For T = 300 K							
	Rho (Kg/m^3)	**Rho***	**P***	**P(MPa)**	**P***	**P (MPa)**	**%**
	34.9720	0.0679	0.1283	5.0436	0.1272	5.0000	0.8728
	75.1750	0.1460	0.2566	10.0873	0.2544	10.0000	0.8728
	155.2800	0.3016	0.5129	20.1628	0.5088	20.0000	0.8138
	271.6900	0.5277	1.2777	50.2280	1.2719	50.0000	0.4561
For T = 400 K							
	Rho (Kg/m^3)	**Rho***	**P***	**P(MPa)**	**P***	**P (MPa)**	**%**
	24.5980	0.0478	0.1277	5.0201	0.1272	5.0000	0.401
	49.7360	0.0966	0.2556	10.0480	0.2544	10.0000	0.4797
	98.5430	0.1914	0.5114	20.1038	0.5088	20.0000	0.519
	203.4300	0.3951	1.2786	50.2634	1.2719	50.0000	0.5268

Figures II.1: Experiments with four different densities conducted in canonical ensemble using L-J model with N= 500 and iterations ranging from 10 to 20 million at 200 K.

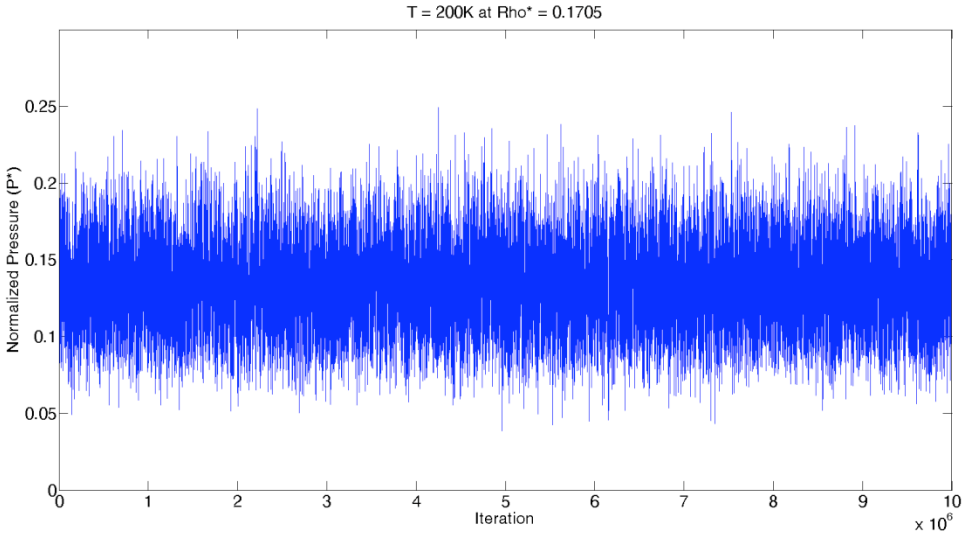

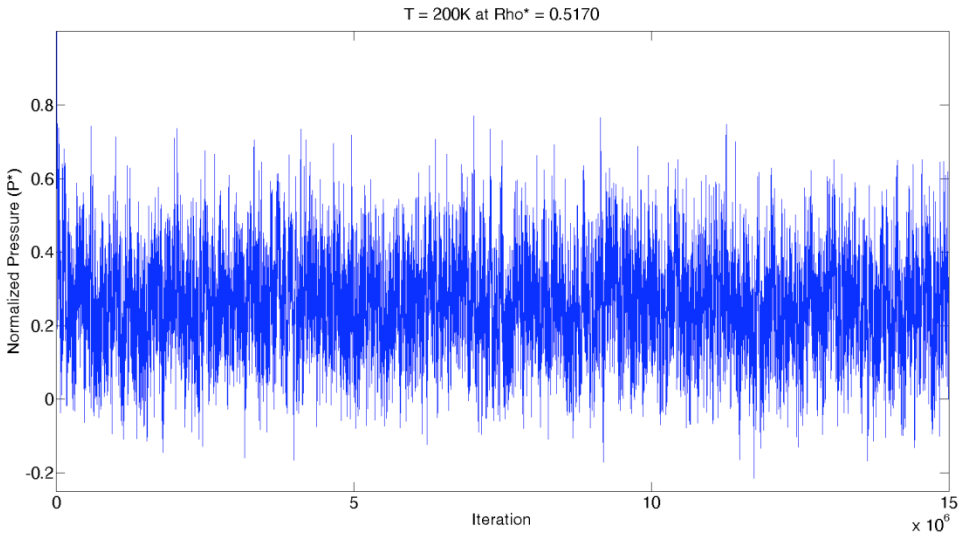

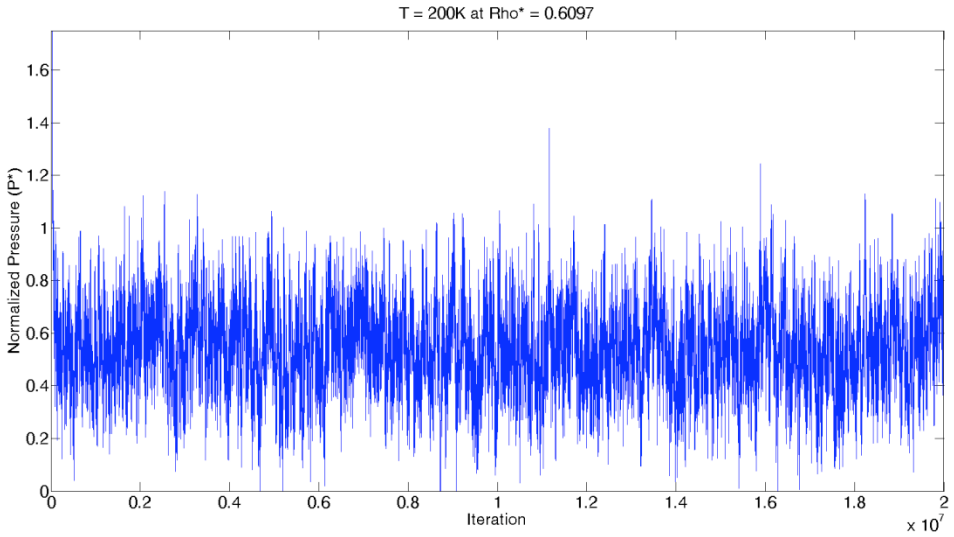
T = 200K at Rho* = 0.6097
Normalized Pressure (P*)
Iteration
x 10^7

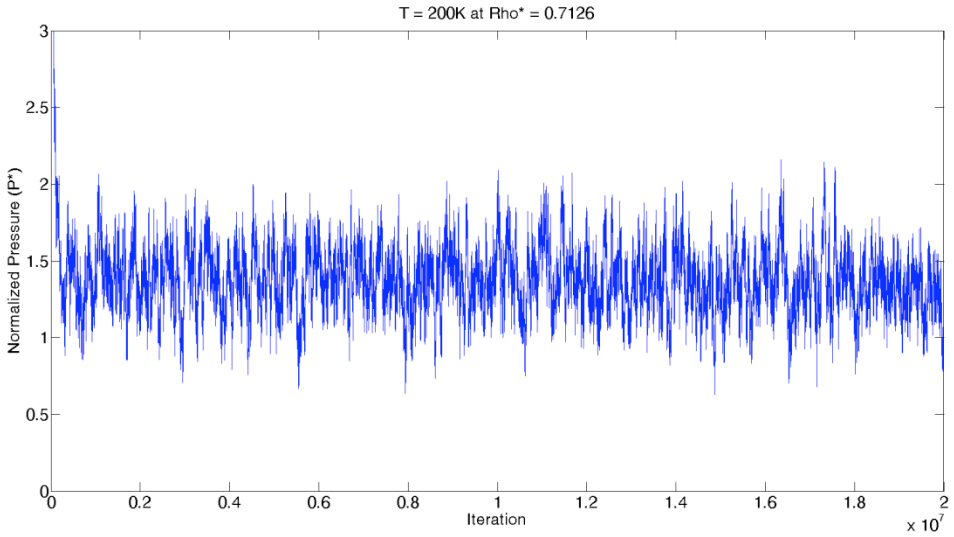
T = 200K at Rho* = 0.7126
Normalized Pressure (P*)
Iteration
x 10^7

Figures II.2: Experiments with four different densities conducted in canonical ensemble using L-J model with N= 500 and iterations ranging from 10 to 20 million at 220 K.

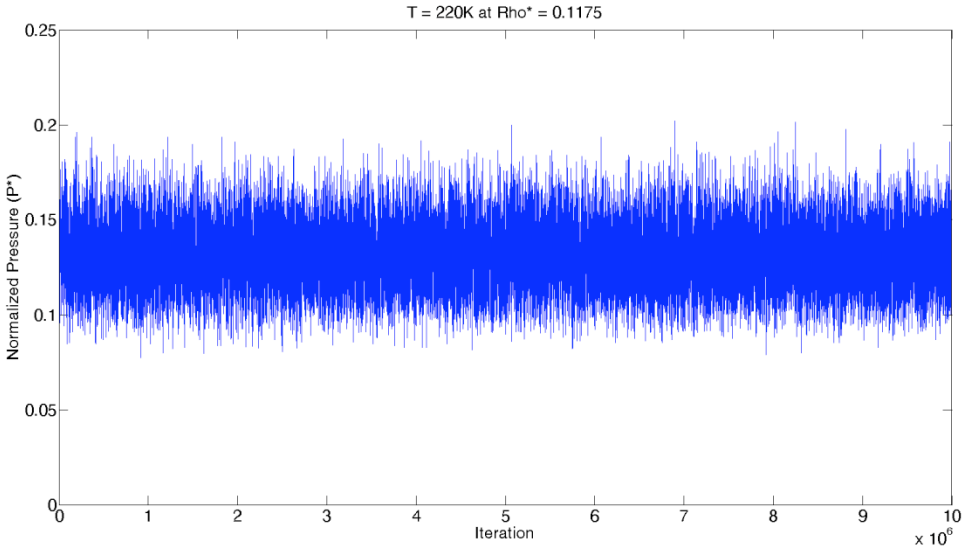

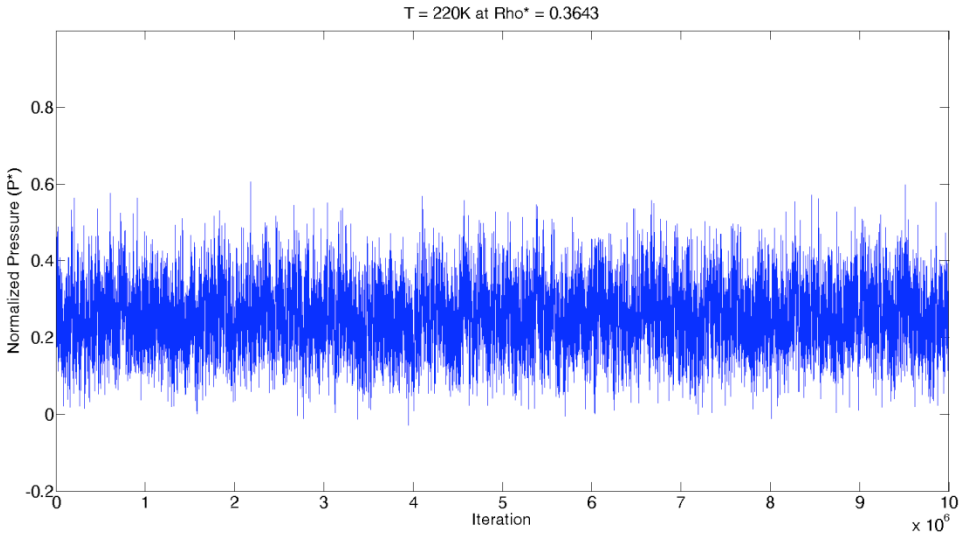

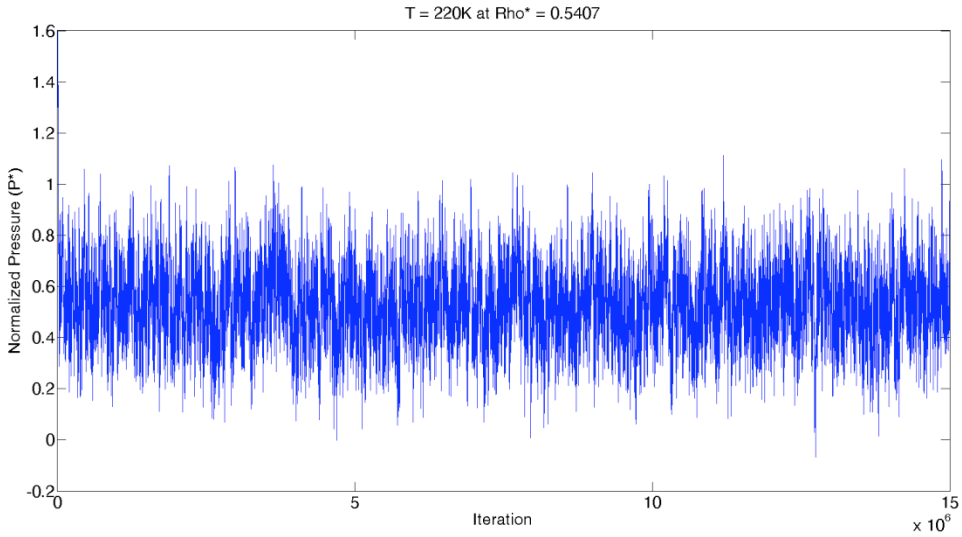
T = 220K at Rho* = 0.5407
Normalized Pressure (P*)
1.6
1.4
1.2
1
0.8
0.6
0.4
0.2
0
-0.2
0
5
10
15
Iteration
x 10^6

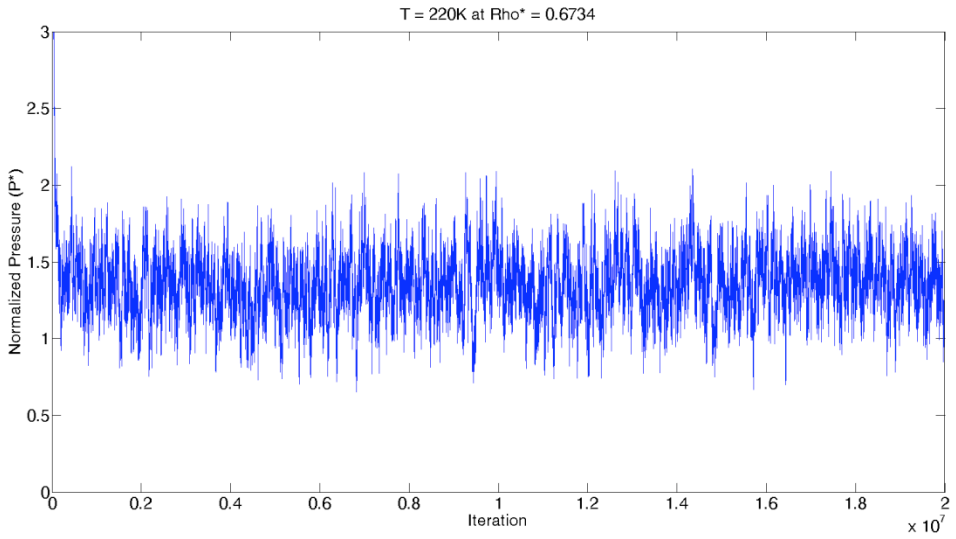
T = 220K at Rho* = 0.6734
Normalized Pressure (P*)
3
2.5
2
1.5
1
0.5
0
0
0.2
0.4
0.6
0.8
1
1.2
1.4
1.6
1.8
2
Iteration
x 10^7

Figures II.3: Experiments with four different densities conducted in canonical ensemble using L-J model with N= 500 and iterations ranging from 10 to 20 million at 250 K.

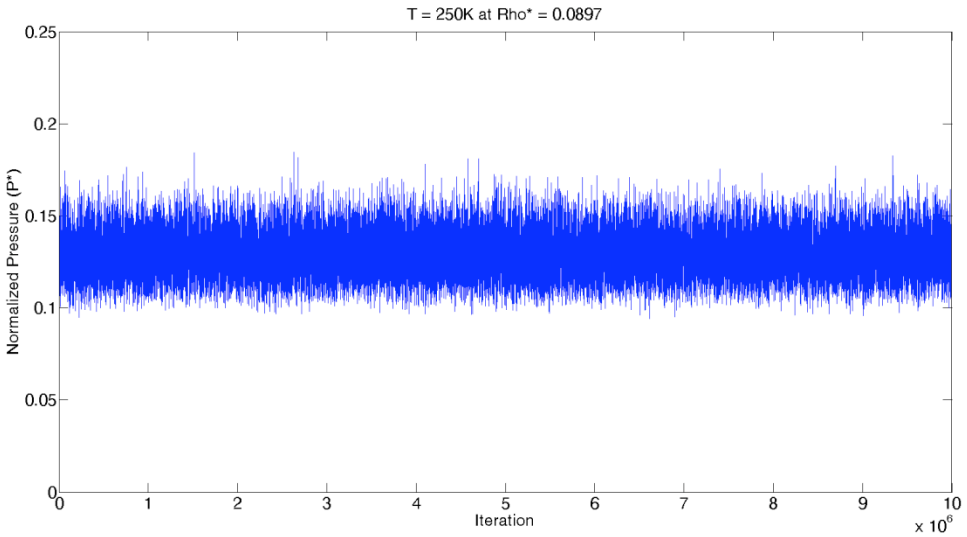

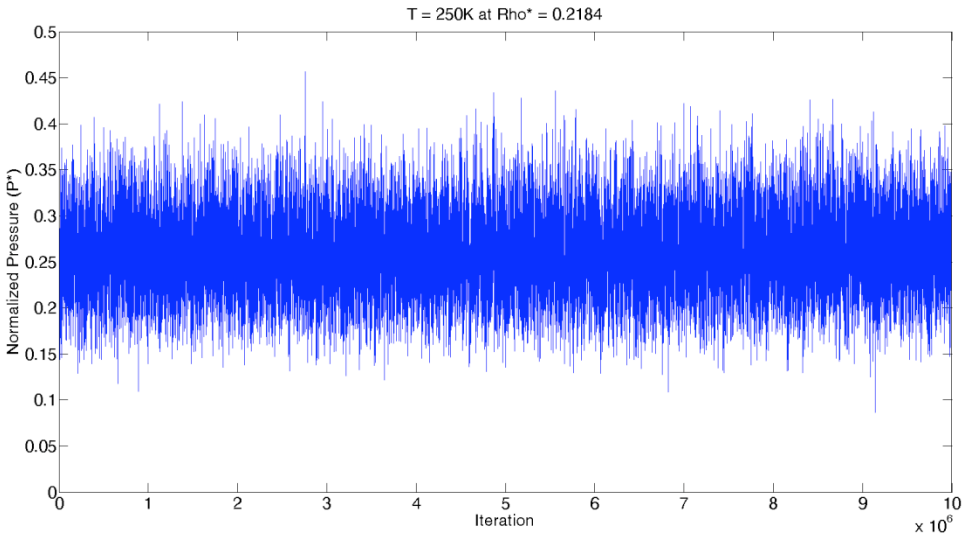

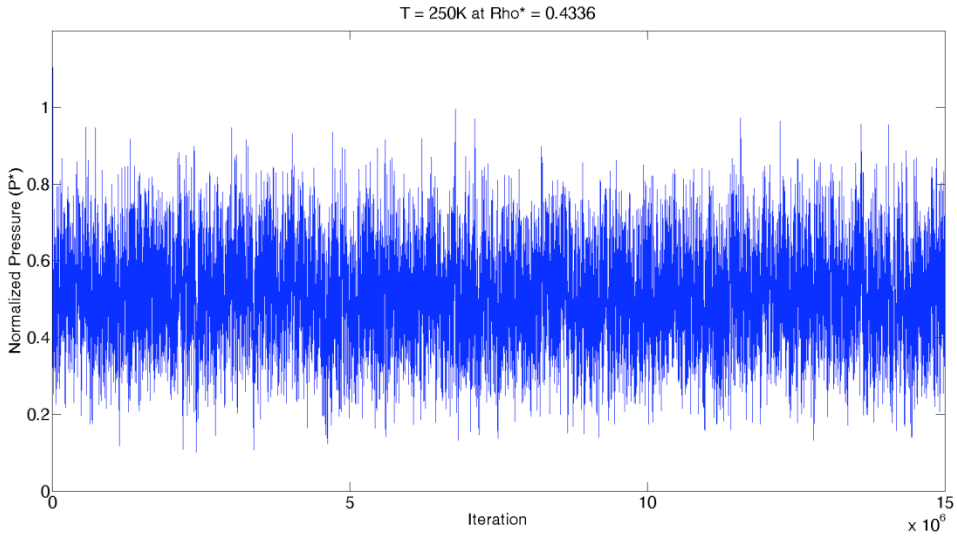
T = 250K at Rho* = 0.4336
Normalized Pressure (P*)
Iteration
x 10^6

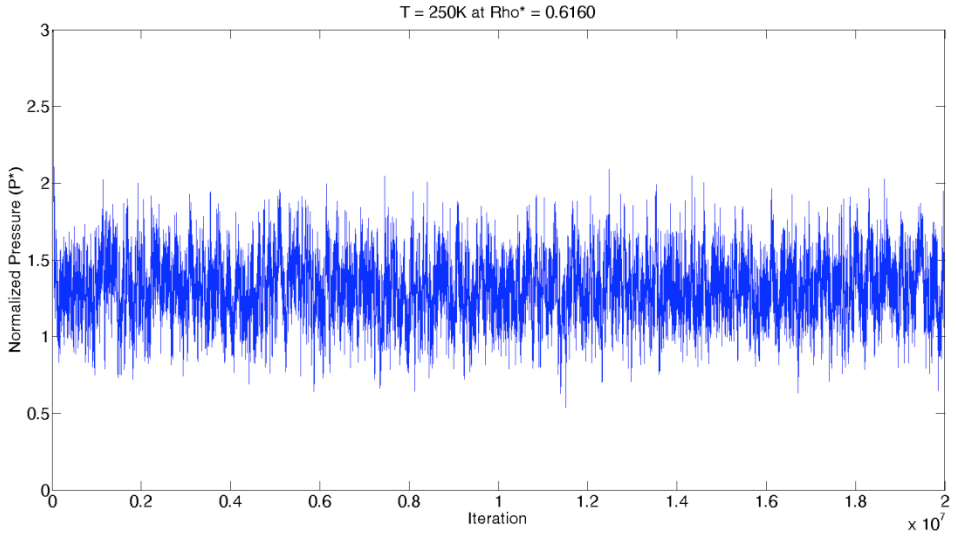
T = 250K at Rho* = 0.6160
Normalized Pressure (P*)
Iteration
x 10^7

Figures II.4: Experiments with four different densities conducted in canonical ensemble using L-J model with N= 500 and iterations ranging from 10 to 15 million at 300 K.

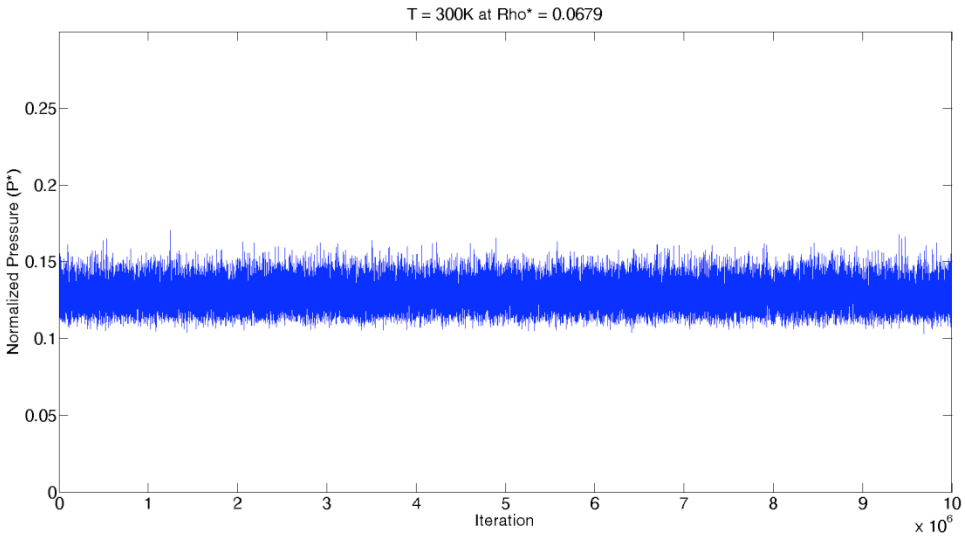

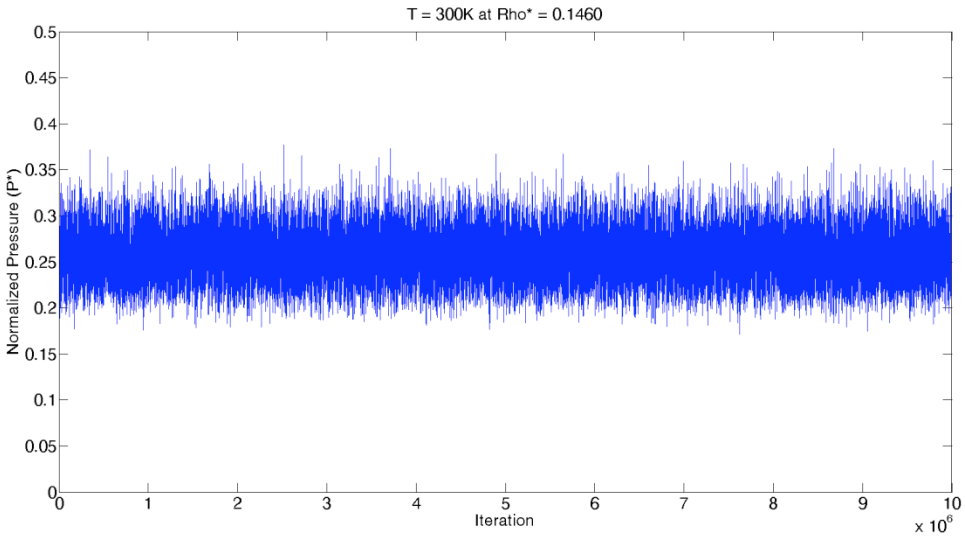

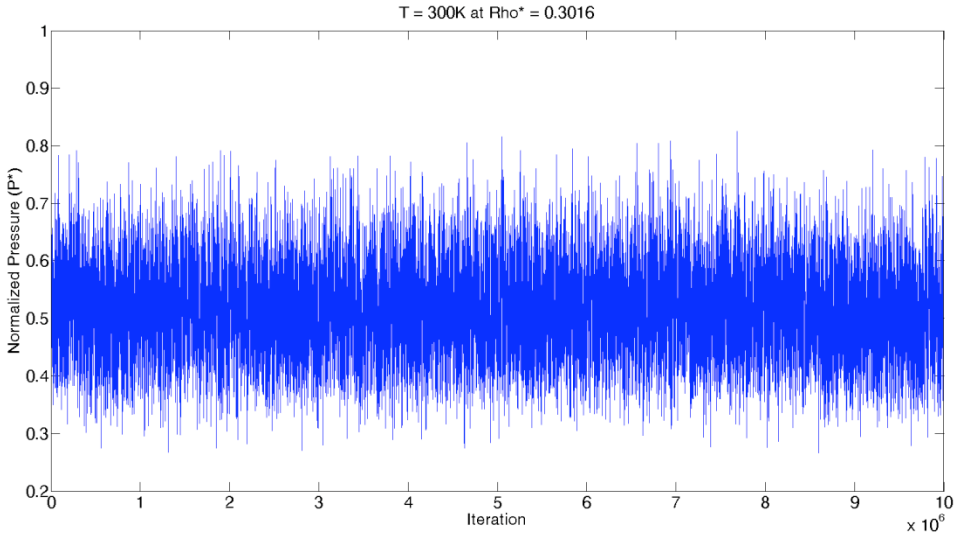
T = 300K at Rho* = 0.3016
Normalized Pressure (P*)
Iteration
x 10^6

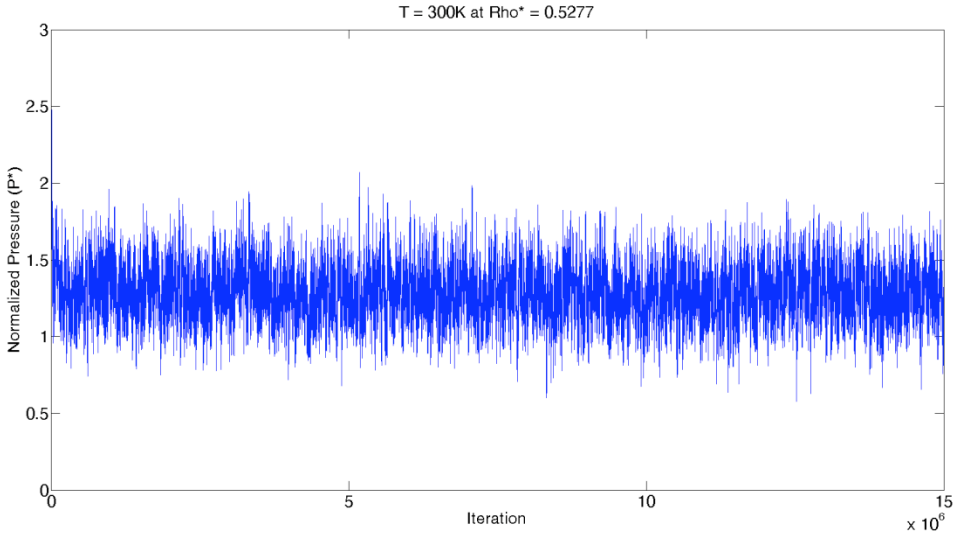
T = 300K at Rho* = 0.5277
Normalized Pressure (P*)
Iteration
x 10^6

Figures II.5: Four experiments with four different densities conducted in canonical ensemble using L-J model with N= 500 and 10 million iterations at 400 K.

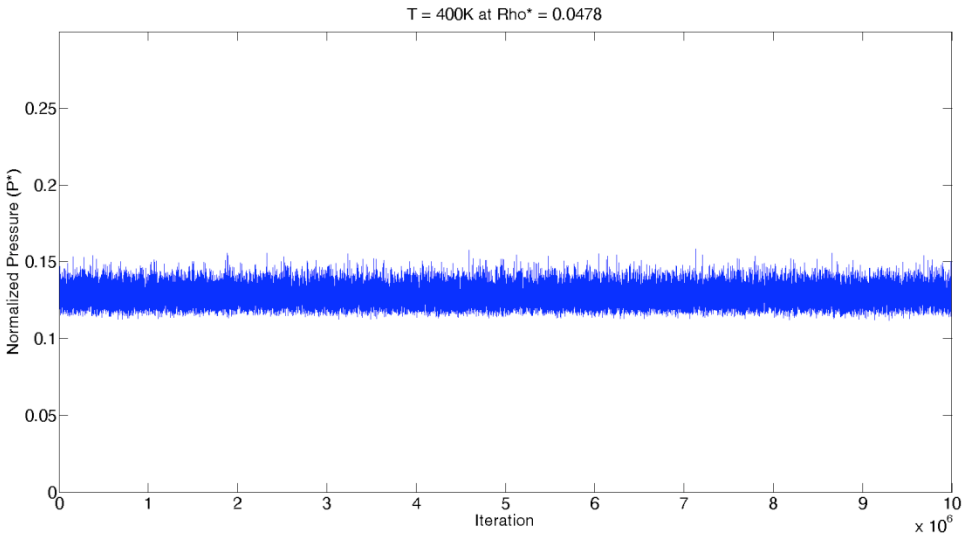

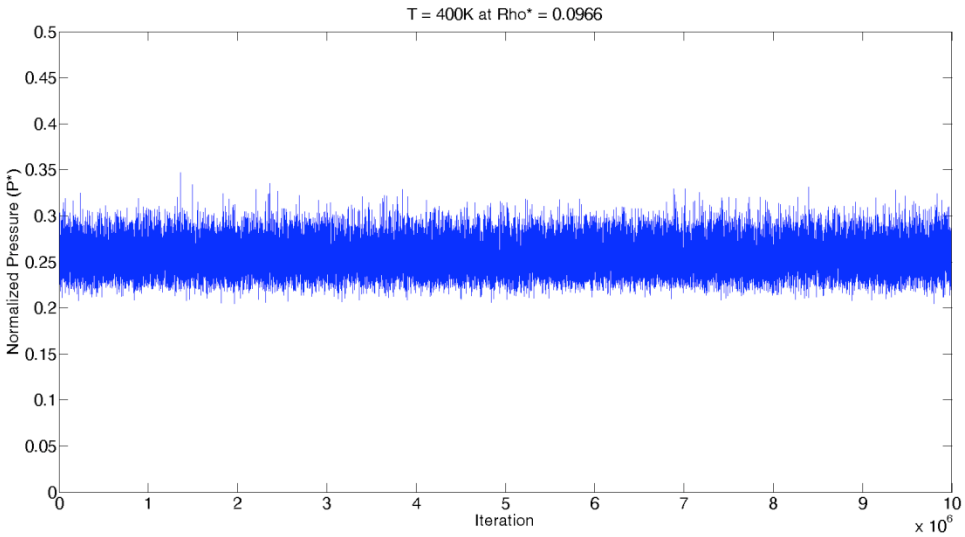

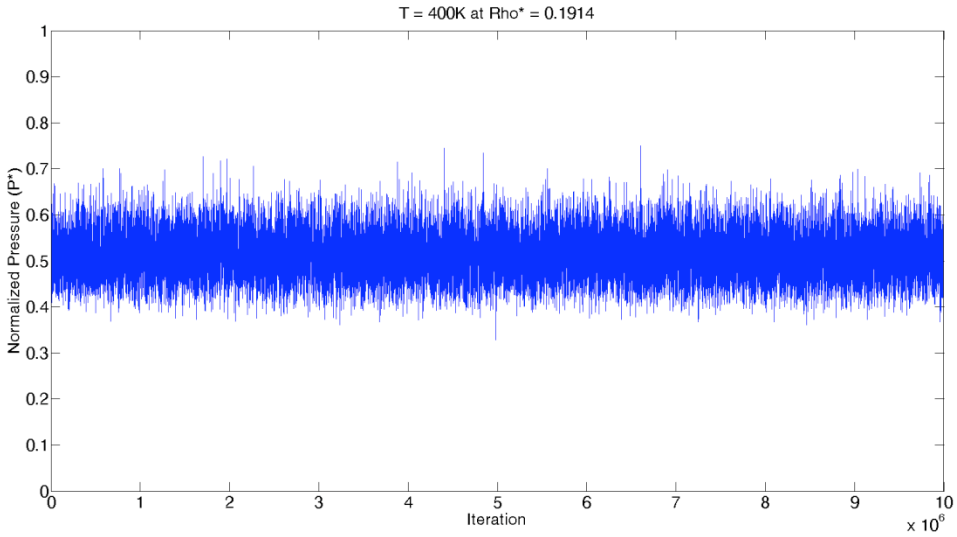
T = 400K at Rho* = 0.1914
Normalized Pressure (P*)
Iteration
x 10^6

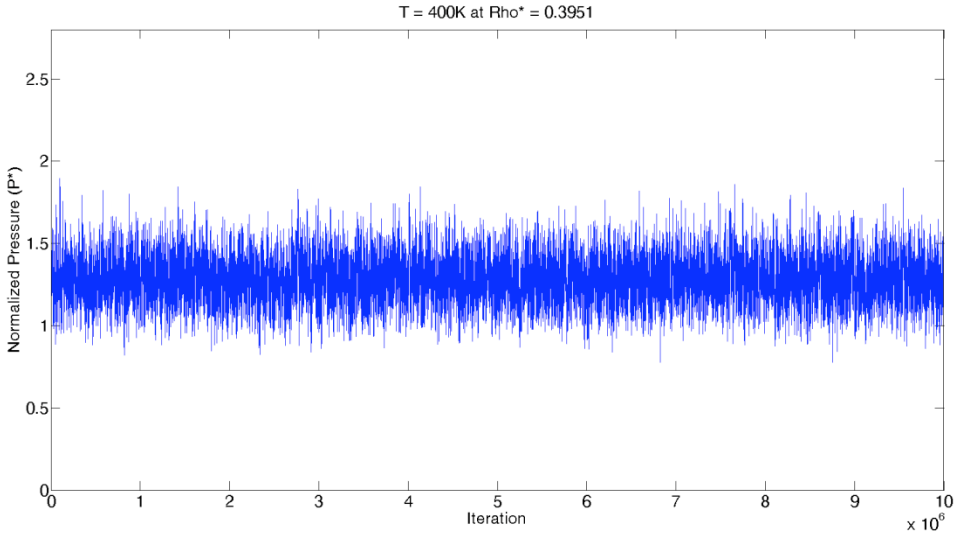
T = 400K at Rho* = 0.3951
Normalized Pressure (P*)
Iteration
x 10^6

Experimental Set III:

Figures III.1-6: Experiments at T = 220 K and normalized density of 0.5407 using L-J potential model in canonical ensemble with six different iterations with MBL factors ranging from 16 to 23 (Total number of iterations = $20*10^6 + 50*2^{MBL}$).

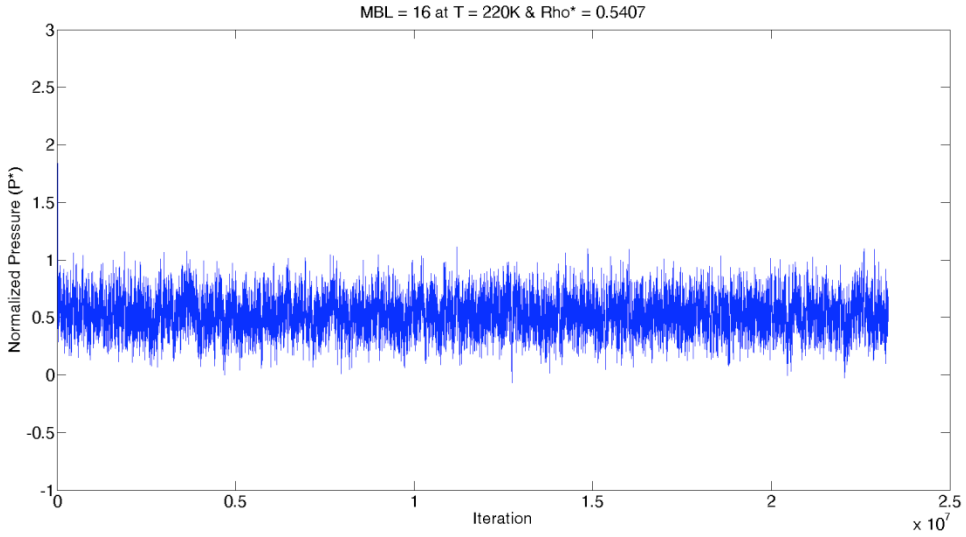

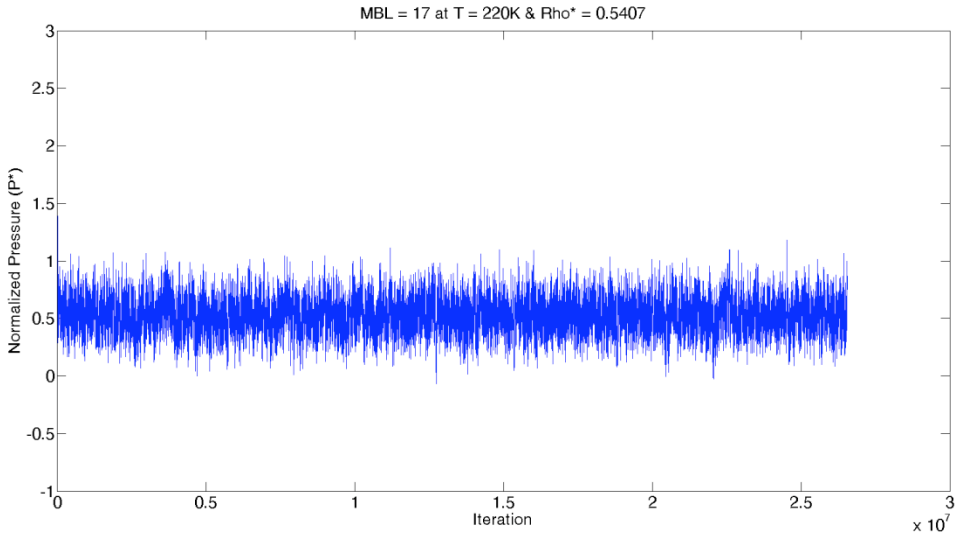

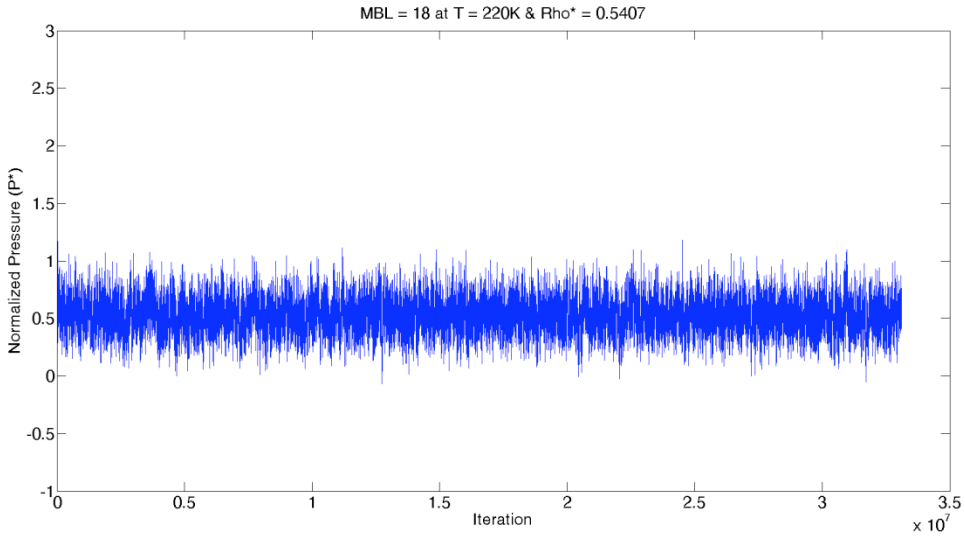
MBL = 18 at T = 220K & Rho* = 0.5407
Normalized Pressure (P*)
Iteration
x 10^7

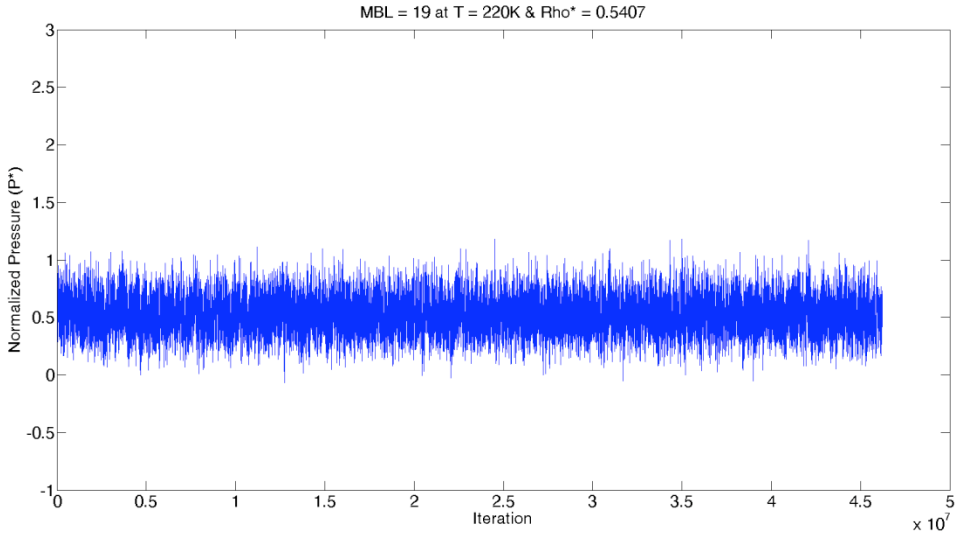
MBL = 19 at T = 220K & Rho* = 0.5407
Normalized Pressure (P*)
Iteration
x 10^7

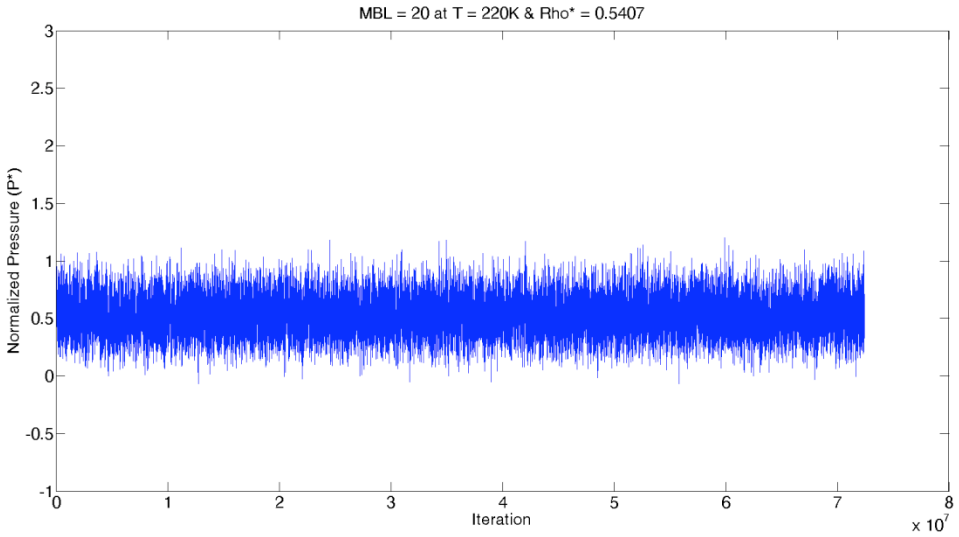
MBL = 20 at T = 220K & Rho* = 0.5407
Normalized Pressure (P*)
Iteration
x 10^7
3
2.5
2
1.5
1
0.5
0
-0.5
-1
0
1
2
3
4
5
6
7
8

Experimental Set IV:

Table IV.1: Summary of data obtained using exp-6 model at different densities and temperature combinations above critical temperature of methane. Collected data is compared to the experimental data obtained by Setzmann and Wagner [104].

Temperature	Density		Simulation Results		Experimental Data		
	Density	Normalized Density	Normalized Pressure	Pressure	Normalized Pressure	Pressure	Error
For T = 200 K							
	Rho in Kg/m^3	Rho*	P*	P(MPa)	P*	P (MPa)	%
	87.7640	0.2426	0.1664	5.0112	0.1660	5.0000	0.2250
	266.1900	0.7359	0.3242	9.7635	0.3321	10.0000	2.3650
	313.9100	0.8679	0.7096	21.3701	0.6641	20.0000	6.8504
	366.9200	1.0144	1.8531	55.8074	1.6603	50.0000	11.6147
For T = 220 K							
	Rho in Kg/m^3	Rho*	P*	P(MPa)	P*	P (MPa)	%
	60.4790	0.1672	0.1622	4.8848	0.1660	5.0000	2.3048
	187.5900	0.5186	0.3247	9.7786	0.3321	10.0000	2.2144
	278.3700	0.7696	0.6738	20.2919	0.6641	20.0000	1.4597
	346.7400	0.9586	1.8351	55.2653	1.6603	50.0000	10.5305
For T = 250 K							
	Rho in Kg/m^3	Rho*	P*	P(MPa)	P*	P (MPa)	%
	46.1590	0.1276	0.1598	4.8125	0.1660	5.0000	3.7503
	112.4300	0.3108	0.3246	9.7755	0.3321	10.0000	2.2445
	223.2300	0.6172	0.6641	19.9998	0.6641	20.0000	0.0009
	317.1500	0.8768	1.8133	54.6088	1.6603	50.0000	9.2175
For T = 300 K							
	Rho in Kg/m^3	Rho*	P*	P(MPa)	P*	P (MPa)	%
	34.9720	0.0967	0.1584	4.7703	0.1660	5.0000	4.5935
	75.1750	0.2078	0.3200	9.6358	0.3321	10.0000	3.6419
	155.2800	0.4293	0.6463	19.4638	0.6641	20.0000	2.6812
	271.6900	0.7511	1.7380	52.3410	1.6603	50.0000	4.6821
For T = 400 K							
	Rho in Kg/m^3	Rho*	P*	P(MPa)	P*	P (MPa)	%
	24.5980	0.0680	0.1580	4.7583	0.1660	5.0000	4.8345
	49.7360	0.1375	0.3161	9.5196	0.3321	10.0000	4.8044
	98.5430	0.2724	0.6354	19.1355	0.6641	20.0000	4.3225
	203.4300	0.5624	1.7680	53.2445	1.6603	50.0000	6.4890

Experimental Set V:

Figures V.1-5: Five experiments at five different temperatures below critical temperature (132, 140, 147, 169, and 183 K) conducted in Gibbs ensemble using L-J model with N= 500 and initial Rho*= 0.3 for both boxes till 20 and 40 million iterations**.**

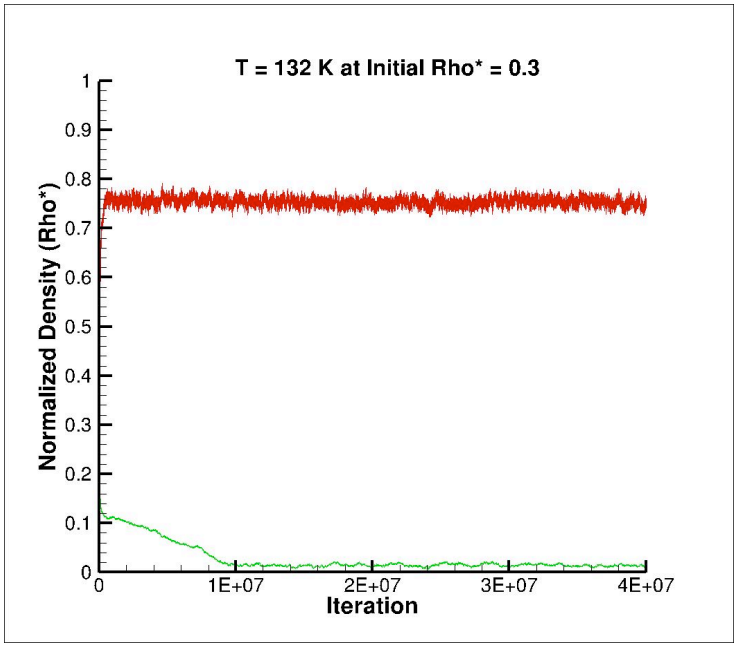

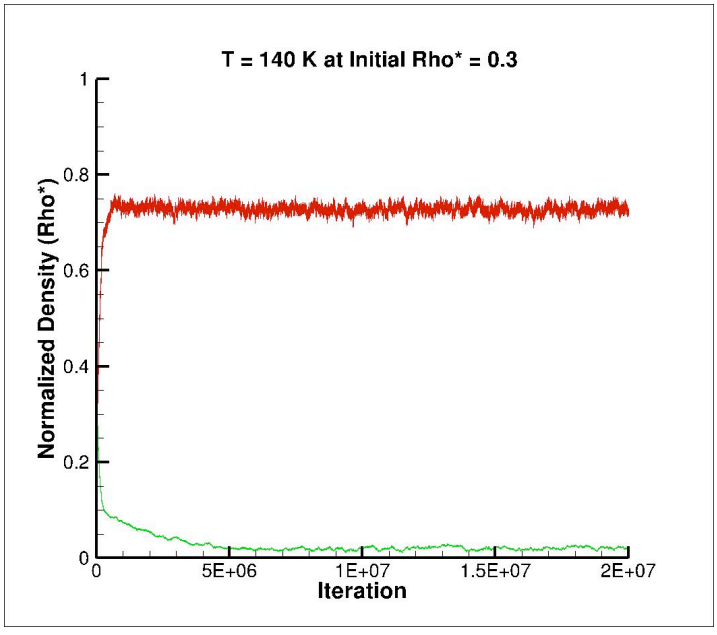

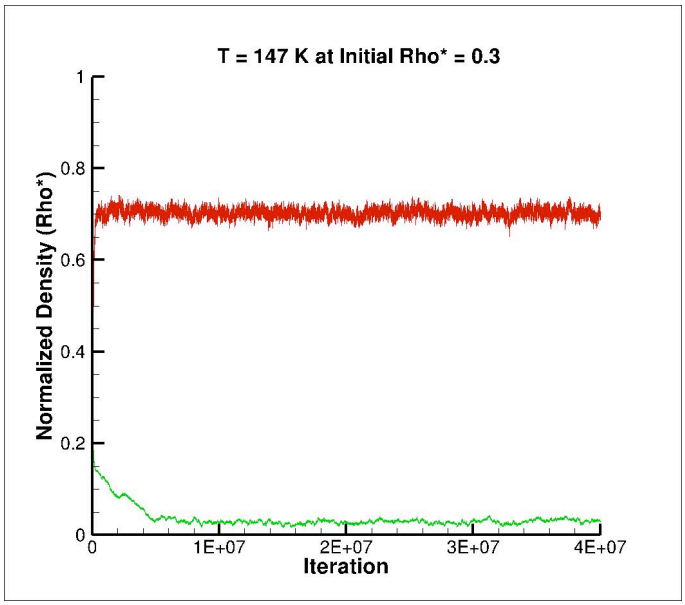
T = 147 K at Initial Rho* = 0.3
Normalized Density (Rho*)
0
0.2
0.4
0.6
0.8
1
0
1E+07
2E+07
3E+07
4E+07
Iteration

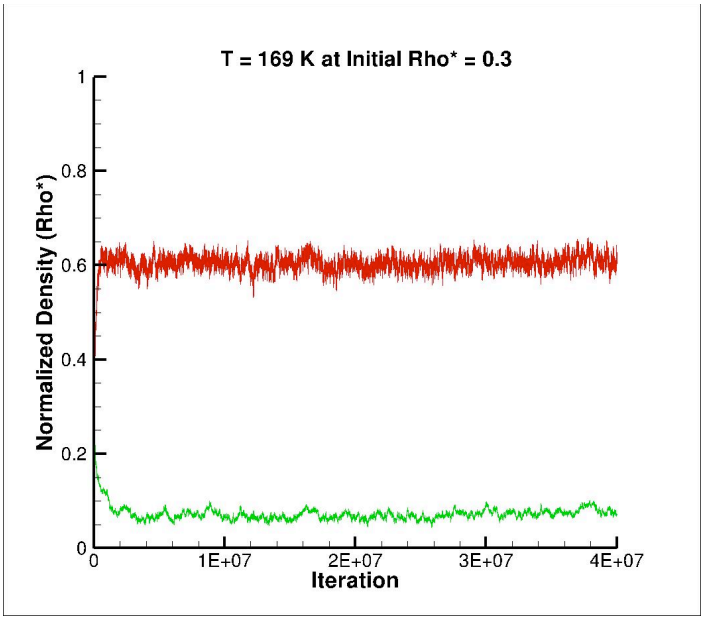
T = 169 K at Initial Rho* = 0.3
Normalized Density (Rho*)
0
0.2
0.4
0.6
0.8
1
0
1E+07
2E+07
3E+07
4E+07
Iteration

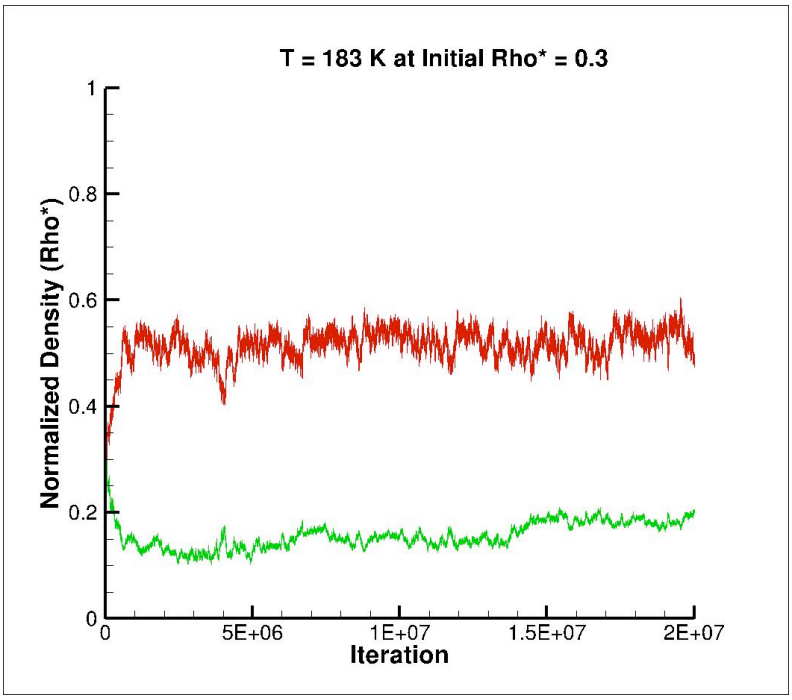

Table V.1: Summary of data obtained using L-J model at different temperatures below critical temperature of methane. Collected data is compared to the experimental data obtained by Setzmann and Wagner [104].

Temprature		Experimental Density		Simulation	Error	Experimental Density		Simulation	Error
T*	T (K)	Rho (Kg/m^3)	Rho*	Rho*	(%)	Rho (Kg/m^3)	Rho*	Rho*	(%)
0.9	132	6.9230	0.0134	0.0146	8.2847	390.7200	0.7589	0.7527	0.8126
0.95	140	10.1520	0.0197	0.0206	4.5772	376.8700	0.7320	0.7278	0.5693
1	147	14.2340	0.0276	0.0295	6.6352	363.8050	0.7066	0.7011	0.7772
1.15	169	37.3660	0.0726	0.0735	1.2770	313.3200	0.6085	0.6062	0.3843
1.25	183	75.8100	0.1472	0.1332	9.5356	257.1400	0.4994	0.5095	2.0175